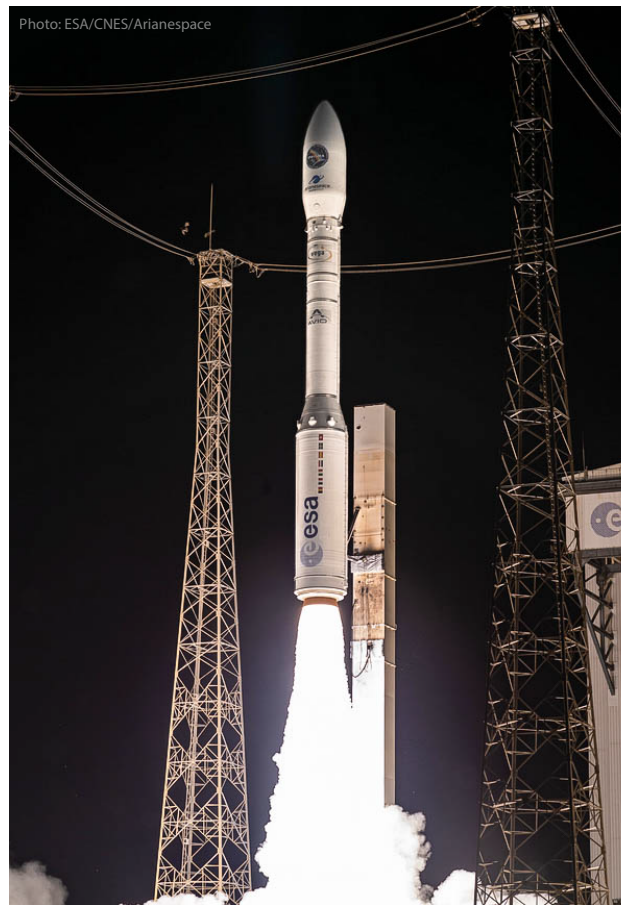


MASTER'S THESIS BY JAKOB STENTOFT POULSEN

Linear Parameter-Varying Control of the VEGA Launch Vehicle

FOURTH SEMESTER OF CONTROL AND AUTOMATION



AALBORG UNIVERSITY

2021



AALBORG UNIVERSITY
STUDENT REPORT

**Fourth Semester | The Technical Faculty
of IT and Design**

Control and Automation

Fredrik Bajers Vej 7

9000 Aalborg

Title:

Linear Parameter-Varying Control
of the VEGA Launch Vehicle

Project:

Master's thesis

Period of Project:

February 1st 2021 - June 3rd 2021

Project Group:

21gr1030a

Members:

Jakob Stentoft Poulsen

Supervisor:

Rafal Wisniewski

External Supervisor:

Finn Ankersen (European Space Agency)

Pedro Simplicio (European Space Agency)

ECTS points: 30

Printed exemplary: 0

Page number: 75

Ended: June 2, 2021

Abstract

The focus of this thesis has been to design a Linear Parameter-Varying (LPV) control system for the European Launch Vehicle (LV) VEGA. More exactly, the objective has been to stabilize the LV during its atmospheric flight from liftoff to Main Engine Cut Off (MECO) when disturbances are present, such as wind gusts, sensor noise and computational delays. The thesis covers a derivation of a 3D LV model and theory, design, and simulation of an LPV controller. The LV model is derived from translational and rotational dynamic equations affecting a six Degrees of Freedom (DoF) LV. The LV is simplified to a 2D model and Jacobian linearizations are conducted in a systematic manner to derive a linear state space representation. This report then establishes well-known requirements for a typical LV during ascent. An LPV controller model is designed with a lower Linear Fractional Transform (LFT) configuration and is augmented with a selection of frequency dependent filters on the input and output channels designed to satisfy the requirements. Lastly, the LV control system is simulated through a linear LPV simulation with user specified inputs. The result from the simulation concludes the LV is stable and is operating as intended while satisfying its requirements.

The content of the report is freely available, but publication (with source reference) may only take place in agreement with the authors.

Preface

This thesis is written by Jakob Stentoft Poulsen, who is studying on the 4th semester of the Control and Automation master's degree on Aalborg University during the spring 2021. The reader of this thesis is therefore assumed to have good knowledge and understanding of control theory.

The author would like to thank Rafal Wisniewski for his frequent help and guidance whenever it was needed throughout the project period.

A thank you also goes out to the European Space Agency (ESA), more specifically to Automatic Control Systems Analyst Finn Ankersen and Systems Engineer Pedro Simplicio from the Guidance, Navigation and Control Section for their supervision and data provision for this project.

Lastly, a special thanks to Frederik Rasmussen for exchanging ideas, discussing concepts and giving inputs during the project.

Table of Contents

1	Introduction	1
1.1	Introduction	1
1.2	Motivation	1
1.3	Outline of the Thesis	4
2	Problem Analysis	6
2.1	VEGA Launch Vehicle Profile	6
2.2	Trajectory	7
2.3	Reference Frames	8
2.4	Dynamic Equations	11
2.5	Aerodynamic Characteristics	12
2.6	TVC Characteristics	15
2.7	Nozzle Dynamics	17
2.8	Flexible-Body Dynamics	18
2.9	Sensor Characterization	21
2.10	Model Linearization	22
2.11	State Space Representation	25
2.12	Uncertainty Modelling	28
2.13	Summary	36
3	Requirement Specification	37
3.1	Technical Requirements	37
3.2	Performance Requirements	37
4	Linear Parameter-Varying Control Design	40
4.1	Introduction to LPV Theory	40
4.2	LPV Modelling	41
4.3	LPV Synthesis	43
4.4	Weighted Interconnection	47
4.5	Weighting Function Selection	49
4.6	Summary	54
5	Results and Analysis	55
5.1	Results	55
5.2	Simulation	56
5.3	Test Conclusion	60
6	Conclusion	61
6.1	Discussion	61
6.2	Conclusion	62

Bibliography	64
A Parameters from Simulation	67

Nomenclature

Acronyms

Abbreviation	Definition
AoA	Angle of Attack
BF	Body-Fixed
CG	Center of Gravity
CP	Center of Pressure
DCM	Direction Cosine Matrix
DoF	Degree of Freedom
ECEF	Earth-Centred Earth-Fixed
ECI	Earth-Centered Inertial
ESA	European Space Agency
HWIL	Hardware-In-the-Loop
INS	Inertial Navigation System
IQC	Integral Quadratic Constraint
LEO	Low Earth Orbit
LMI	Linear Matrix Inequality
LPV	Linear Parameter-Varying
LTI	Linear Time Invariant
LV	Launch Vehicle
MECO	Main Engine Cut Off
MIMO	Multiple-Input and Multiple-Output
SDP	Semidefinite Programming
SECO	Second Engine Cut Off
SSO	Sun Synchronous Orbit
TVC	Thrust Vector Control
TWD	Tail-Wags-Dog
VEGA	Vettore Europeo di Generazione Avanzata
VF	Velocity-Fixed

Symbols

Symbol	Definition	SI-unit
β_{TVC}	Thrust vector control actuator deflection	[rad]
τ	Time delay	[s]
θ, θ_y	Pitch angle	[rad]
θ_z	Yaw angle	[rad]
$\dot{\theta}$	Pitch rate	[rad/s]
$\ddot{\theta}$	Pitch acceleration	[rad/s ²]
ρ_{air}	Air density	[Pa]
ζ	Dampening ratio	[·]
ω_{q_i}	Natural frequency of the i^{th} bending mode	[rad]
Ψ_t^{PVP}	Translational bending mode length at the nozzle pivot point	[m]
Ψ_r^{PVP}	Rotational bending mode length at the nozzle pivot point	[rad]
Ψ_r^{INS}	Translational bending mode length at the sensor location	[m]
Ψ_r^{INS}	Rotational bending mode length at the sensor location	[rad]
C_x, C_y, C_z	DCM for x, y and z from ECI frame to BF frame	[·]
$C_{X \rightarrow Y}$	DCM for transforming from X-frame to Y-frame	[·]
\ddot{r}	Acceleration	[m/s ²]
m	Launch vehicle mass	[m]
$F_{\#}$	Force of $\#$ acting on the launch vehicle	[N]
$M_{\#}$	Moment of $\#$ acting on the launch vehicle	[N · m]
J, J_y	Moment of inertia	[kg · m ²]
$x_{\#}$	x -coordinate of $\#$ on the launch vehicle	[m]
$P_{\#}$	Point location of $\#$ on the launch vehicle	[·]
$\alpha, \alpha^{CP}, \alpha_{eff}$	Angle of attack and effective angle of attack	[rad]
β, β^{CP}	Sideslip angle	[rad]
v_w	Crosswind acting on the launch vehicle	[m/s]
v_{total}^{CP}, v_{air}	Total wind velocity and headwind acting on the CP	[m/s]
V	Air relative velocity CP in the BF frame	[m/s]
v_x	Longitudinal velocity	[m/s]
Q	Dynamic pressure aerodynamic load indicator	[Pa]
$Q_{\alpha, total}, Q_{\alpha}$	Aerodynamic load indicator	[Pa · deg]
S_{ref}	Reference aerodynamic area	[m ²]
CD, CL, CN	Drag, lift and normal launch vehicle force coefficients	[·]

M	Mach number	[·]
L_w	Turbulence scale	[m]
σ_w	standard deviation of wind turbulence	[m/s]
V_w	Vertical wind profile	[m/s]
$\ddot{\beta}$	Acceleration of the nozzle actuator	[deg/s ²]
m_N	Mass of the LV nozzle.	[m]
l_N	Distance from the nozzle center of gravity to nozzle pivot point	[m]
J_N, J_y	Moment of inertia of nozzle about pivot point and for y-axis	[kg · m ²]
q_i	State of the i th bending mode	[m]
L	Is the length of the vehicle	[m]
r_{INS}	Position of sensor on the launch vehicle	
l_{INS}	Distance between sensor location and center of gravity	[m]
$J_{\#}$	Jacobian matrix for # state space matrix	
$\#_0$	Operating point for # parameter	
z	Lateral drift w.r.t. the reference trajectory in the pitch plane	[m]
σ_x, δ_x	Standard deviation for parameter x and bounded uncertainty flag	[·]
x^0	Nominal value of parameter x	[·]
$\Delta_{\#}$	Diagonal uncertainty block for # parameter(s)	
I_{\bullet}	Identity matrix with number \bullet as size	[·]
n_w	White noise transfer function	[·]
$\mathcal{F}_l, \mathcal{F}_u$	Upper and lower LFT operations	
$0_{m \times n}$	Zero matrix of dimension n by m	
$\rho(t)$	Time-varying parameter	
\mathcal{L}_2	Space of signals with finite 2-norm	
$\ \mathcal{T}_{zw}\ _{\mathcal{L}_2 \rightarrow \mathcal{L}_2}$	Closed-loop \mathcal{L}_2 norm from exogenous input to exogenous output	[·]
γ	\mathcal{L}_2 -norm upper bound gain	[·]
W_i, W_o	Diagonal matrices with input weight and output weights	
S, T	Sensitivity and complementary sensitivity transfer functions	
M, P, G, K	Generalised closed-loop and open-loop plant, subsystem and controller.	

1.1 Introduction

Modern society is so heavily embossed by the wireless communication between everyday electronically devices and satellites, that it is hard to imagine living without it. The almost instantaneous transmission time between devices from all over the Earth makes it possible to communicate with whoever at any time with various services. These services include among other telephones, internet, TV, GPS and weather forecasts. Overall, these services have one thing in common, they are transmitting signals via a satellite. Without transmitting signals via a satellite, the wireless communication is limited to local signal coverage. Satellites will continue to contribute to the modern society even more in the future, not only on Earth, but also for interplanetary communication. However, putting a satellite into orbit with a Launch Vehicle (LV), has proven to be a challenging process. In the following section, some of the challenges and why it is such a difficult process will be elaborated upon.

1.2 Motivation

Since the late fifties, the odds for an LV to have an error to classify it as a failure is approximately one in ten [1]. Critical failures include e.g., not reaching the desired orbit in general or losing communication with the LV and payload. Statistically speaking, these odds have been improved since the first satellite was launched into space. In Table 1.1 the success rate for all LVs has been listed for each decade since the first satellite, Sputnik 1, have been successfully put into orbit by the Soviet Union.

Period [year]	Success rate [%]
1957-1959	48.70
1960-1969	78.06
1970-1979	93.45
1980-1989	95.31
1990-1999	92.71
2000-2009	94.09
2010-2019	94.82
Total	89.37

Table 1.1: LV success rate per decade [1] [2]

This table shows that the decade between 1980-1989 has the highest success rate of putting launchers into space. According to [2] and [3], that was also the decade with most recorded

launches. In Figure 1.1 an overview of every LV launched into orbit by country are shown. It is clear by the data that during the Cold War, the Soviet Union was responsible for most of the launches.

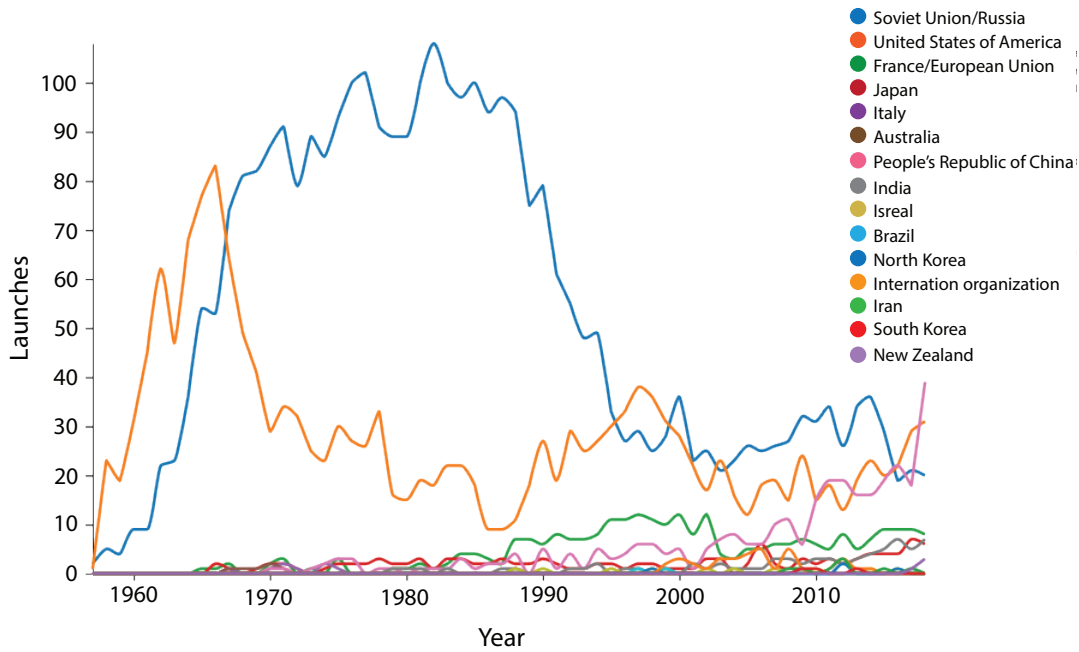


Figure 1.1: Graphs showing the number of orbital launches by country [3] [4]

To dive deeper into what makes it so difficult to put a satellite into orbit, an insight into which part of the LV which causes the most problems have been made. In [5], a statement was made that from an analysis by Aerospace Corporation that most known launch failures, are mainly from three causes: Engine failure, stage-separation failure, and avionics failure. This statement is also in compliance with [6], which is an investigation of catastrophic failures of LVs. This investigation presents data of number of times that subsystems have caused a critical failure for LVs from its time published. This data can be seen below in Figure 1.2

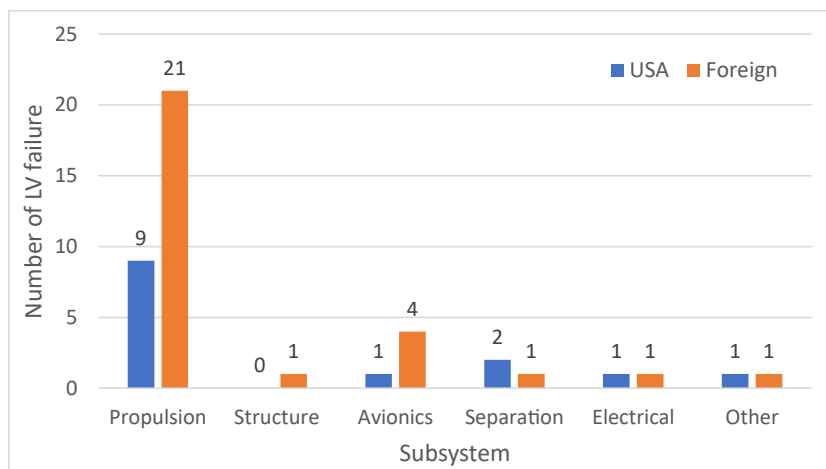


Figure 1.2: Graph showing number of times subsystems have caused an LV failure [6]

Where *Propulsion* includes most notably of main propulsion components of the LV engine, nozzle and thrust vector actuator and gimbal mechanism. *Structure* consist of solid rocket motor core support structures, fuel tank storage and payload fairing. *Avionics* contains onboard software, gyro, attitude sensors and navigation and guidance control equipment. *Separation* includes staging of LVs. *Electrical* contains e.g. electrical power supply. *Other* relates to communication and environment etc. [6].

The graph shows the that the propulsion subsystem is the main course for LV failure, where the avionics and stage separation subsystems are the second and third main causes, respectively.

When analyzing the subsystem errors mentioned in Figure 1.2, the majority of the failures are occurring in the very first phase in every ascent profile of LVs, i.e. the atmospheric phase from liftoff to MECO. In fact, the phase when the LV is flying through the atmosphere, is the most difficult task to overcome of its journey to space [7]. This is because the avionics and propulsion system work together against Earth's gravitational field to not only gain a high enough altitude, but also a high enough horizontal velocity to stay in orbit. This task is made substantially more challenging because of Earth's atmosphere puts a great deal of structural load on the LV as the velocity increases [8]. At around halfway up through the atmosphere, the dynamic pressure will be at its highest (max-Q) and the avionic system will have to steer the nozzle such that the LV experiences as little pressure as possible. If the structural load becomes too high, the LV will simply not be able to handle the pressure.

Figure 1.3 presents a simplified overview of a typical ascent profile for an LV. The first phase starts from liftoff and ends at Main Engine Cut Off (MECO). From there, the second stage will ignite and continue to carry the payload until Second Engine Cut Off (SECO). Depending on the LV, a couple of stage separations will continue to happen but will eventually end with a payload deployment when the desired altitude and velocity has been reached [9].

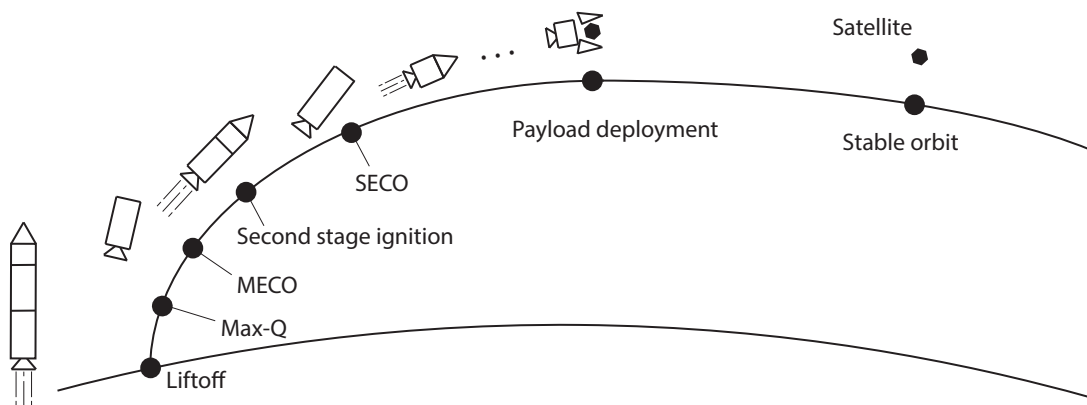


Figure 1.3: A simplified ascent profile for an LV from liftoff to operational orbit

In the next section an outline for the rest of thesis is presented.

1.3 Outline of the Thesis

This thesis is motivated by increasing the reliability of LVs successfully deploying satellites into orbit. In the previous section, it was concluded that propulsion systems together with avionic systems, are main causes of LV failures. Further it was concluded that the most challenging part of the ascent is the atmospheric phase, that is from liftoff to MECO.

This thesis will, in collaboration with European Space Agency (ESA), cover a derivation of the non-linear dynamics for a full three-dimensional LV model. These dynamics are then used to derive a family of linearized 2D models, which are used to design a controller to stabilize the non-linear LV model.

The controller will be designed from the family of derived linearized models with well-known stability and performance requirements considered. With better reliability of LVs in mind, an uncertain propulsion subsystem, delay model and disturbance model will be accounted for as well as a wind disturbance model. Furthermore, uncertain dynamics in the LV model will be analyzed as well.

Additionally, the dynamics for the LV model are expected to change with time as the LV ascents through the atmosphere, e.g., mass, velocity, air density, etc. To encapsulate all the varying parameters that make out the dynamics, an optimal choice of controller will be a Linear Parameter-Varying (LPV) controller. An LPV controller will ensure a better dynamical solution to the upcoming resulting control problem.

To make a robust LPV synthesis, theory for Integral Quadratic Constraints (IQC) must to get implemented. Theory about IQC has been considered out of scope for this thesis and robust LPV synthesis will therefore not be conducted. If robust control had to get conducted an \mathcal{H}_∞ -controller could be considered. This type of controller is supported by MATLAB via the Robust Control Toolbox [10]. However, it has been chosen to in depth with on LPV control and not focus on other types of controllers.

For this project, the Vettore Europeo di Generazione Avanzata (VEGA) LV will be used as a benchmark to get an accurate representation of a real LV as possible. Here, the dimensions of VEGA's various components are adopted together with model-specific parameters.

1.3.1 Simulation and Data

The parameter values used for the LV model, have either been acquired from ESA or generated by a partly non-linear six Degree of Freedom (DoF) simulation described in [1]. This non-linear simulation does not support bending modes, nor the Tail-Wags-Dog (TWD) effect later described in this project. However, when compared with data from other VEGA mission profiles in [11], the simulation data is assumed to be a sufficient approximation for this thesis. The data obtained from this simulation is from liftoff at zero seconds to a hundred seconds (right before MECO) with a total resolution of 4996 data points. The data from the simulation used in this project can be seen in Appendix A.

Ideally, the resulting closed-loop system would be tested in a complete non-linear

simulation, but this has not been considered a prioritization for the scope of this thesis and will therefore not be made. Instead, an LPV simulation from the toolbox *LPVTools* will be conducted [12] [13]. The results will be analyzed up against the requirements by testing the closed-loop model in the simulation.

Lastly, the full 3D linearization of the LV model, LPV controller and simulation from this thesis have been added to a public GitHub repository [14]. Note that the parameter values acquired from ESA have not been included at their request.

Problem Analysis 2

This chapter will cover the relevant topics and analyses for finally a deriving a linearized 2D model of an LV.

First and foremost, this chapter will present an overview of the VEGA LV mission profile and dimensions followed by a description of a typical trajectory profile. Before describing the relevant dynamics, the necessary reference frames are analyzed in Section 2.3. From there on, all the rigid-body- and flexible body dynamics used in the full 3D non-linear model are deduced and presented in their respective reference frames. Jacobian linearization is then used to linearize the model and is described as two-dimensional model at different equilibrium points along a preprogrammed trajectory. Lastly, Linear Fractional Transform (LFT) theory will then be presented and the 2D LV model together with a TVC actuation model and delay model will then be described in an upper LFT configuration.

2.1 VEGA Launch Vehicle Profile

VEGA is the lightweight launch vehicle under responsibility of ESA and European Launch Vehicle (ELV), where the latter is the prime contractor. VEGA is the smallest European launch vehicle with a height of thirty meters, a diameter of three meters (see Figure 2.1) and weights 138 ton [15]. The VEGA LV is designed to carry relatively small payloads from 300 kg to 2500 kg [15]. The orbits that VEGA is carrying the payloads up to are either Low Earth Orbit (LEO) or Sun-Synchronous Orbit (SSO). LEOs are at altitudes between 160- to 1000 km, but are usually in the lower end of the altitude interval. SSOs are between 600- and 800 km. Satellites in SSOs are placed in a polar orbit arranged such that it passes the same spot on Earth the same time every day [16].

VEGA consists of four stages, where the first stage is P80. The P80 is a solid-fuel stage designed to burn for 114 seconds and achieve a relative velocity of 1.7 km/s. The stage is jettisoned (MECO) at around 53 km altitude depending on the mission [17]. Besides the first stage, there are Zefiro 23, Zefiro 9 and AVUM which corresponds to the second, third and fourth stage, respectively. These stages are activated beyond MECO, so they are not in the scope of this thesis and thus will be considered as payload henceforth. In Table 2.1 is an overview of the different stages showing the dimensions and average thrust force.

Stages	Stage 1: P80	Stage 2: Zefiro 23	Stage 3: Zefiro 9	Stage 4: AVUM
Height [m]	11.7	7.5	3.5	1.7
Diameter [m]	3	1.9	1.9	1.9
Propellant type	Solid	Solid	Solid	Fluid
Propellant mass [t]	88	24	10.5	0.55
Motor dry mass [kg]	7330	1950	915	131
Average thrust [kN]	2200	871	260	2.42
Burn time [s]	114	77	120	667
Specific impulse [s]	280	287.5	296	315.5

Table 2.1: Parameters of the different stages on the Vega LV [1] [18]

On the P80 stage the Thrust Vector Control (TVC) system is located. During the atmospheric ascent phase, the TVC system stabilizes the LV by gimbaling a movable nozzle with two electromechanical actuators. The TVC system gets its data from measurements from the Inertial Navigation System (INS) located as shown in Figure 2.1 [19].

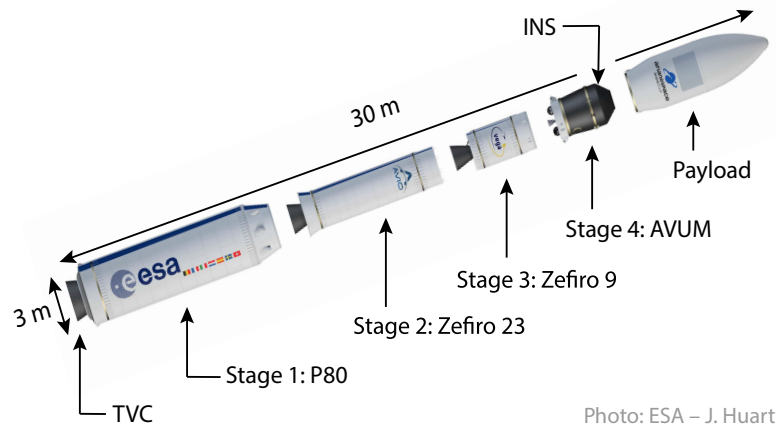


Figure 2.1: VEGA launch vehicle and its components [1]

2.2 Trajectory

The LV is set to follow a preprogrammed trajectory before launch. However, during the atmospheric phase of the flight, a crucial objective for the LV is to alleviate the structural load that originate from the aerodynamic forces. This is the reason why the guidance system is configured in an open-loop during the atmospheric phase, so that the LV can deviate from the preprogrammed trajectory in order to reduce the Angle of Attack (AoA) and thereby reduce the structural load in presence of wind disturbances. Later in Section 2.5 a performance indicator for this structural load will be introduced. Naturally, using an open-loop configuration introduces the trade-off that the LV deviate from the reference trajectory. Any final deviations from the reference trajectory is corrected with closed-loop guidance in non-atmospheric phases beyond MECO [19].

The pitch- and yaw angle (θ_y and θ_z) for the LV for the first 110 seconds of a typical atmospheric flight has been provided by ESA and can be seen in Figure 2.2. Later in

Section 2.6 the planned thrust is presented for the atmospheric phase, when introducing the TVC dynamics.

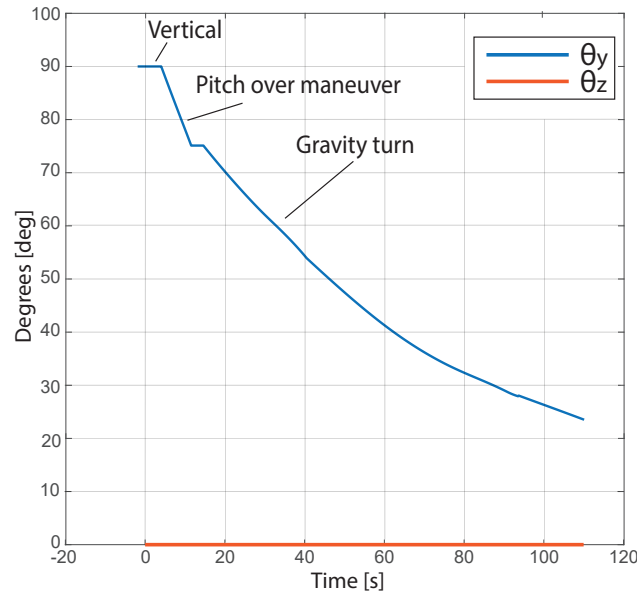


Figure 2.2: Pitch and yaw angle for a typical trajectory provided by ESA

In Figure 2.2 the pitch angle relative to the ground is 90° in the first four seconds. This is to avoid any collision with the launch pad. After four seconds, a relatively small pitch over maneuver is initiated for approximately twelve seconds. The maneuver is made so that the gravitational pull can tip the LV over for the remainder of the flight, which is also presented in the figure. This gravitation pull is called a gravity turn. The gravity turn is made to give the LV horizontal velocity naturally without any actuation efforts from the TVC system while keeping the AoA close to zero [19] [1]. These practical advantages of the gravity turn will be utilized later when choosing the operating points for linearization in subsection 2.10.1. The yaw angle is relative to the pitch plane and is theoretically zero throughout the flight.

At the time of MECO the VEGA LV should have made a downrange of 64 km due to the gravity turn [20].

2.3 Reference Frames

Before describing the dynamics of the LV, the reference frames are important to have defined beforehand. When describing the motion of an object in space, it is considered practical to describe it through an inertial reference frame. Additionally from a control perspective, it can be practical to use the object that is being controlled as the frame of reference. Below are various reference frames explained which are essential for describing the six DoF dynamic model of an LV. These reference frames are also explained in [8]. In Figure 2.3, the upcoming reference frames are illustrated.

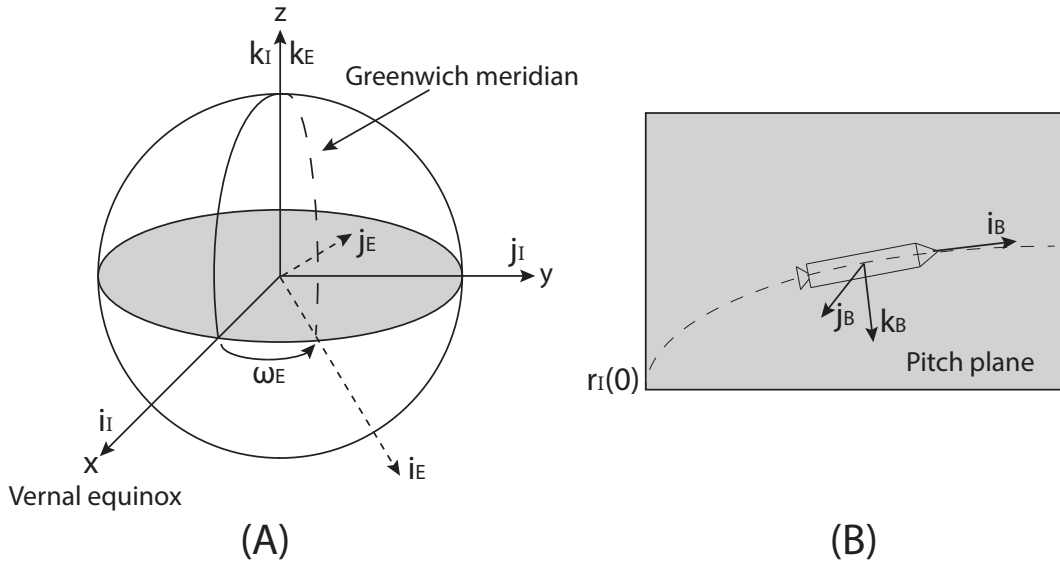


Figure 2.3: Illustrations of different reference frames. (A) shows the ECI- and ECEF frames and (B) shows the BF frame [1]

Earth-Centered Inertial Reference Frame

The Earth-Centered Inertial (ECI) reference frame can be thought of having its orientation fixed to the motionless universe around it. It has its origin at the center of the Earth, with the set of basis vectors $\{i_I, j_I, k_I\}$, where i_I points at the Sun during vernal equinox at spring, k_I points at the North Pole and j_I completes the right-handed coordinate set. Vernal equinox is when the Sun is directly above the equator of the Earth.

Earth-Centered Earth-Fixed Frame

The Earth-Centered Earth-Fixed (ECEF) frame has the same origin and equatorial plane as with the ECI frame. It is defined by the set of vectors $\{i_E, j_E, k_E\}$, where i_E is now fixed on the Greenwich meridian. k_E and j_E are oriented the same way as before in the ECI frame, where k_E points towards the North Pole and j_E completing the right-handed coordinate set. This means this frame rotates with the Earth's angular velocity corresponding to $\Omega_I = \omega_E k_I$, where $\omega_E = 0.7292 \cdot 10^{-6}$ rad/s is the rotational velocity of the Earth [21].

In this thesis, the simulations from the six DoF simulation described in subsection 1.3.1, are initiated from Europe's Spaceport located in Kourou, French Guiana. Thereby, the initial starting point and initial velocity can be calculated by applying the latitude, longitude and altitude: $r(0) = \{\psi(0), \lambda(0), h(0)\} \approx \{5.2^\circ, -52.8^\circ, 0 \text{ m}\}$.

Body-Fixed Reference Frame

The Body-Fixed (BF) frame has its origin at the LV's Center of Gravity (CG). This frame is useful when describing LV rotations and will be used when defining the CG, Center of Pressure (CP), nozzle Pivot Point (PVP) and other mass and aerodynamic properties later in this thesis. The BF frame is defined by the set of vectors $\{i_B, j_B, k_B\}$, where i_B is

pointing along the LV longitudinal axis, k_B is perpendicular on the yaw plane while j_B is perpendicular to the LV's pitch plane completing the right-handed coordinate set.

To transform one coordinate from one reference frame to another reference frame a Direction Cosine Matrix (DCM) can be used. A DCM transforms one coordinate reference frame to another. Equation 2.1, 2.2 and 2.3 are DCMs and represent the transformation of the x , y and z -axis from the ECI reference frame to the BF reference frame, respectively.

$$C_x = \begin{bmatrix} 1 & 0 & 0 \\ 0 & \cos \theta_x & \sin \theta_x \\ 0 & -\sin \theta_x & \cos \theta_x \end{bmatrix} \quad (2.1)$$

$$C_y = \begin{bmatrix} \cos \theta_y & 0 & \sin \theta_y \\ 0 & 1 & 0 \\ -\sin \theta_y & 0 & \cos \theta_y \end{bmatrix} \quad (2.2)$$

$$C_z = \begin{bmatrix} \cos \theta_z & \sin \theta_z & 0 \\ -\sin \theta_z & \cos \theta_z & 0 \\ 0 & 0 & 1 \end{bmatrix} \quad (2.3)$$

For the rotational sequence of $C_z(\theta_z) \leftarrow C_y(\theta_y) \leftarrow C_x(\theta_x)$ yields the DCM from ECI frame to BF frame given in Equation 2.4 [22].

$$C_{I \rightarrow B} = \begin{bmatrix} \cos(\theta_y) \cos(\theta_z) & \cos(\theta_x) \sin(\theta_z) - \cos(\theta_z) \sin(\theta_x) \sin(\theta_y) & \sin(\theta_x) \sin(\theta_z) + \cos(\theta_x) \cos(\theta_z) \sin(\theta_y) \\ -\cos(\theta_y) \sin(\theta_z) & \cos(\theta_x) \cos(\theta_z) + \sin(\theta_x) \sin(\theta_y) \sin(\theta_z) & \cos(\theta_z) \sin(\theta_x) - \cos(\theta_x) \sin(\theta_y) \sin(\theta_z) \\ -\sin(\theta_y) & -\cos(\theta_y) \sin(\theta_x) & \cos(\theta_x) \cos(\theta_y) \end{bmatrix} \quad (2.4)$$

Velocity-Fixed Reference Frame

For describing the aerodynamic characteristics later in Section 2.5, a Velocity-Fixed (VF) frame is necessary. The basis set of vectors are $\{i_V, j_V, k_V\}$. Here the frame is also fixed to the LV's CG, but with i_V pointing along the direction relative to the air velocity. Below is the DCM for transforming from VF frame to BF frame [8].

$$C_{V \rightarrow B}(t) = \begin{bmatrix} \cos \alpha(t) \cos \beta(t) & \sin \beta(t) & \sin \alpha(t) \cos \beta(t) \\ -\cos \alpha(t) \sin \beta(t) & \cos \beta(t) & -\sin \alpha(t) \sin \beta(t) \\ -\sin \alpha(t) & 0 & \cos \alpha(t) \end{bmatrix} \quad (2.5)$$

Where α is the AoA and β is the sideslip angle, they will be elaborated upon in Section 2.5.

Now that the necessary reference frames have been explained, the dynamic equations for an LV are described.

2.4 Dynamic Equations

This section presents an overview of the dynamics of the LV that are described by the standard six DoF equations of motion which consist of translational and rotational dynamics. Both the translational and rotational dynamics are summarized below, and their complete derivation can be found in [23]. Each component of both equations is evaluated in the sections to come in this chapter. Furthermore, sloshing effect and jet damping have not been considered for these equations.

The LV's translational motion is described in Equation 2.6 in the ECI frame.

$$m(t)\ddot{r}_I(t) = F_{aero}(t) + F_{TVC}(t) + F_N + F_F(t) + F_g(t) \quad (2.6)$$

where:

$\ddot{r}_I(t)$	is the acceleration.	$\left[\frac{m}{s^2} \right]$
$m(t)$	is the mass of the vehicle.	$[kg]$
$F_{aero}(t)$	is the aerodynamic force acting on the vehicle.	$[N]$
$F_{TVC}(t)$	is the thrust vector control acting on the vehicle.	$[N]$
$F_N(t)$	is the force from accelerating the nozzle actuator.	$[N]$
$F_F(t)$	is the elastic body force acting on the vehicle.	$[N]$
$F_g(t)$	is the gravitational force acting on the vehicle.	$[N]$

Additionally, the rotational dynamics are described in the BF frame in Equation 2.7.

$$J(t)\ddot{\theta}_B(t) = M_{aero,B}(t) + M_{TVC,B}(t) + M_{N,B}(t) + M_{F,B}(t) + M_{g,B} \quad (2.7)$$

where:

$\ddot{\theta}(t)$	is the angle acceleration with partitioning: $[\ddot{\theta}_x \ \ddot{\theta}_y \ \ddot{\theta}_z]^T$	$\left[\frac{rad}{s^2} \right]$
$J(t)$	is the moment of inertia	$[kgm^2]$
$M_{aero}(t)$	is the aerodynamic moment acting on the vehicle.	$[Nm]$
$M_{TVC}(t)$	is the thrust moment acting on the vehicle.	$[Nm]$
$M_N(t)$	is the nozzle moment acting on the vehicle.	$[Nm]$
$M_F(t)$	is the elastic body moment acting on the vehicle.	$[Nm]$
$F_g(t)$	is the gravitational momentum acting on the vehicle.	$[Nm]$

Note that the rotational motion of the LV happens around its CG. The moment of force is calculated by taking the cross product between the force and moment arm (the distance from where the force is applied to the CG):

$$M = F \times (P_F - P_{CG}) \quad (2.8)$$

where P_F is the point on the LV where the force is applied and P_{CG} is the point on the LV where the CG is. The notation of a specific point P is in this thesis expressed by a 3D vector on the form: $P = [x \ y \ z]^T$.

In the following sections, the parts of the translational and rotational dynamics are explained and evaluated upon in the following order: Aerodynamic characteristics, TVC forces, dynamics of the nozzle, flexible-body dynamics (elastic forces) and sensor placement characteristics.

2.5 Aerodynamic Characteristics

Throughout this section various concepts related to aerodynamics relevant for an LV are going to be explained. First the concept of center of pressure will be explained as this is fundamental for the concepts yet to come. Then the total wind velocity is explained followed by the angle of attack and sideslip. The dynamic pressure is then described before explaining the actual aerodynamic force and momentum introduced in the previous section. Lastly, a performance indicator between the angle of attack and dynamic pressure is introduced.

When describing an aerodynamic force acting across the surface of a body, the total amount of force can be accumulated into a single point called the Center of Pressure (CP). All aerodynamic characteristics are therefore described in relation to the CP.

The LV's relative air velocity in the BF reference frame is given by its velocity, $v_{air} = [v_x(t) \ v_y(t) \ v_z(t)]^T$. When the LV is rotating, the body will get affected by a crosswind which is stronger the further away from the CG that is being evaluated from. In Equation 2.9, the total wind including rotational crosswind and regular crosswind at the CP is described.

$$v_{total}^{CP}(t) = v_{air}(t) + \underbrace{\dot{\theta}_B(t) \times (P_{CP} - P_{CG})}_{\text{Rotational crosswind}} + \underbrace{v_w(t)}_{\text{Crosswind}} \quad (2.9)$$

where $\dot{\theta}_B(t) = [\dot{\theta}_{x,B}(t) \ \dot{\theta}_{y,B}(t) \ \dot{\theta}_{z,B}(t)]^T$ and $v_w(t) = [v_{w,x}(t) \ v_{w,y}(t) \ v_{w,z}(t)]^T$.

An essential concept when describing the aerodynamic forces, is how the LV's body is oriented w.r.t. to the wind. The orientation is described with two angles, AoA and sideslip at the CP.

$$\alpha^{CP}(t) = \arctan_2 \left(\frac{v_{total,z}^{CP}(t)}{v_{total,x}^{CP}(t)} \right) \quad (2.10)$$

$$\beta^{CP}(t) = \arcsin \left(\frac{v_{total,y}^{CP}(t)}{v_{total}^{CP}(t)} \right) \quad (2.11)$$

where AoA is α and is the angle between the longitudinal axis of the LV's body and the local airflow at the CP in the pitch plane, and the sideslip angle is β and is the angle between the longitudinal axis and the local airflow in the yaw plane. Visualizations of the AoA and the sideslip angle are illustrated in Figure 2.4.

The aerodynamics forces and moments generated by the LV's main body depend on the external shape and the dynamic pressure. The dynamic pressure is given by:

$$Q(t) = \frac{1}{2} \rho_{air}(t) V^2(t) \quad (2.12)$$

where:

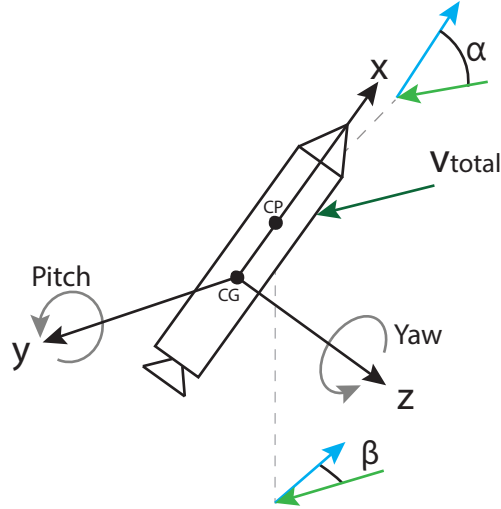


Figure 2.4: Visualization of how the angle of attack, α , and sideslip angle, β , is measured compared to an LV. The blue and the green arrows are the projected longitudinal axis and air velocity at the CP both in the yaw and pitch plane [1].

$$\begin{array}{l} Q(t) \\ \rho_{air}(t) \\ V(t) \end{array} \left| \begin{array}{l} \text{is the dynamic pressure.} \\ \text{is the atmospheric density} \\ \text{is the air relative velocity at the LV's CP in BF frame} \end{array} \right. \begin{array}{l} [\text{Pa}] \\ [\frac{\text{kg}}{\text{m}^3}] \\ [\frac{\text{m}}{\text{s}}] \end{array}$$

where the air relative velocity vector is given by: $V(t) = \|v_{total}^{CP}(t)\|$.

The VEGA launcher is assumed to have an axisymmetric shape. By utilizing this knowledge, the aerodynamic force in the VF reference frame can be described as:

$$F_{aero,V} = -Q(t)S_{ref} \begin{bmatrix} C_D(\alpha_{eff}(t), M(t)) \\ 0 \\ C_L(\alpha_{eff}(t), M(t)) \end{bmatrix} \quad (2.13)$$

where S_{ref} is a reference aerodynamic area and C_D and C_L are the drag and lift coefficients, respectively. The drag and lift coefficients are estimated as functions of the effective angle of attack, $\alpha_{eff}(t)$, and the Mach number, $M(t)$. They are given in Equation 2.14 and Equation 2.15, respectively.

$$\alpha_{eff}(t) = \arccos \left(\cos(\alpha^{CP}(t)) \cos(\beta^{CP}(t)) \right) \quad (2.14)$$

$$M(t) = \frac{V(t)}{V_{sound}(t)} \quad (2.15)$$

where $V_{sound}(t)$ is the speed of sound at the given atmospheric density, $\rho_{air}(t)$.

The data on the aerodynamic coefficients is provided by ESA. These coefficients are for a full configuration of the VEGA LV from 0° to 12° of effective angle of attack. In Figure 2.5 approximations on the coefficients can be seen as a function of α_{eff} at different Mach

numbers. Note that when α_{eff} goes below zero, C_L will keep decreasing. (The graphs are symmetric around $C_L = 0$.) Meanwhile C_D is increasing when α_{eff} goes below zero. (The graphs are symmetric around $\alpha_{eff} = 0$.)

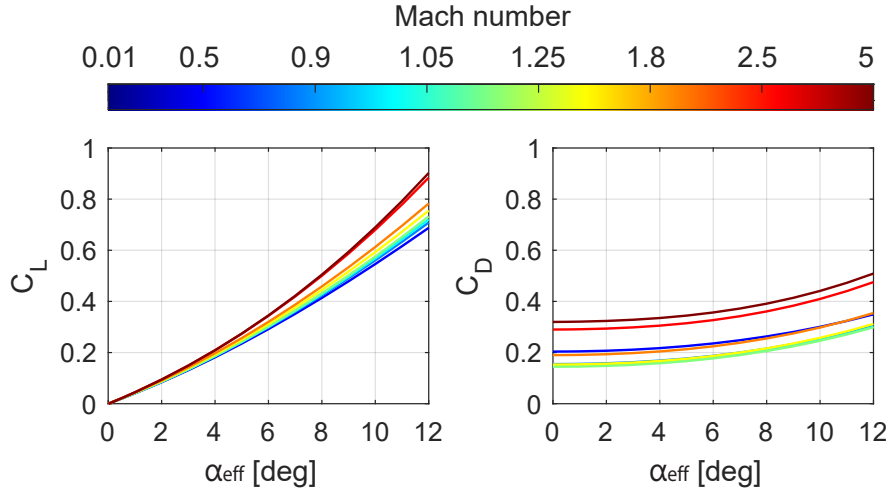


Figure 2.5: Aerodynamic coefficients for a VEGA LV

The data has been approximated by the least squares method and the functions will be interpolated between according to whichever Mach number is closest to the corresponding data.

In Equation 2.16 is the normal aerodynamic coefficient described. This coefficient is the sum of the two normal force from C_L and C_D w.r.t. the longitudinal axis of the LV.

$$C_N(\alpha_{eff}(t), M(t)) = C_L(\alpha_{eff}(t), M(t)) \cos \alpha_{eff}(t) + C_D(\alpha_{eff}(t), M(t)) \sin \alpha_{eff}(t) \quad (2.16)$$

In Figure 2.6 C_L , C_D and C_N are visualized. C_N is the sum of the two blue stippled lines generated from C_L and C_D . C_N will be a relevant parameter in Section 2.10 when the 3D model is linearized.

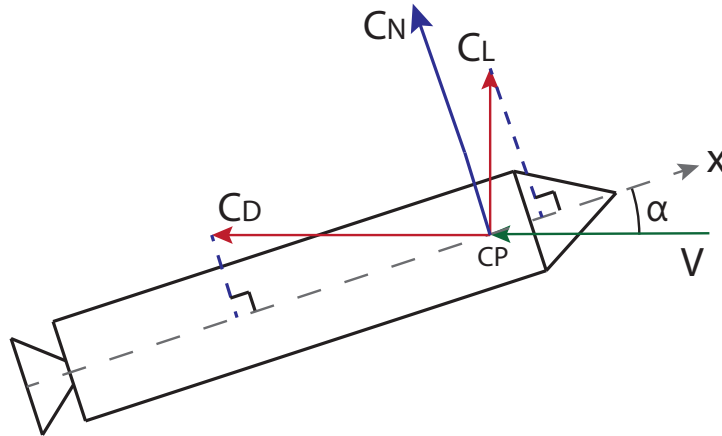


Figure 2.6: Sketch that shows the relationship between C_N , C_L and C_D

Furthermore, the aerodynamic moment around the CG can be computed from the cross product between the force and the two points CG and CP:

$$M_{aero,B} = (P_{CP} - P_{CG}) \times (C_{V \rightarrow B}(t) F_{aero,V}) \quad (2.17)$$

A performance indicator Q_α is also introduced here:

$$Q_\alpha(t) = Q(t) \cdot \alpha_{eff}(t) \quad (2.18)$$

This is a useful indicator as it directly evaluates the impact of trajectory and attitude on induced loads [8]. Later in the requirement specification in Section 3.2, this indicator will further be evaluated upon as this is desired to be kept as low as possible [8] [1].

Since the Q_α is desired to be measured, it will be included in the C-matrix in the state space representation of the LV that is later derived in Section 2.11. This means in order to model the Q_α , it has to be expressed by rotational and translational variables, since they are going to be the states of the state space representation.

Q_α is dependent on the rotation and velocity through $\alpha_{eff}(t)$. In Equation 2.19 and Equation 2.20 is $\alpha_{eff}(t)$ shown dependent on rotational and translational motion, respectively. The dependence on time t has been omitted for better readability.

$$\alpha_{eff}(\theta_y, \theta_z) = \theta_y + \theta_z \quad (2.19)$$

$$\alpha_{eff}(v_{total,y}^{CP}, v_{total,z}^{CP}) = \frac{v_{total,y}^{CP} + v_{total,z}^{CP}}{v_{total}^{CP}} \quad (2.20)$$

Finally, the total dynamic pressure is then given in Equation 2.21.

$$Q_{\alpha,total} = Q \left(\alpha_{eff}(\theta_y, \theta_z) + \alpha_{eff}(v_{total,y}^{CP}, v_{total,z}^{CP}) \right) \quad (2.21)$$

Summary

Through this section, the concepts of center of pressure, total wind velocity, angle of attack, sideslip, effective angle of attack, dynamic pressure, translational force, rotational momentum and Q_α have been explained. All these concepts will be used when building the final model of the LV.

The next section will describe the characteristics of the main engine mounted on the LV.

2.6 TVC Characteristics

The main engine generates the necessary thrust for the LV to enter the required altitude for MECO. As mentioned in Section 2.1, the LV has two electromechanical actuators that operate the movable nozzle in two directions in the BF reference frame: $\{\beta_{TVC,y} \beta_{TVC,z}\}$. The two actuators are assumed to be attached 90° apart, and are defined such that $\beta_{TVC,y}$ is rotating around the y-axis and $\beta_{TVC,z}$ is rotating around the z-axis in the BF frame.

This concept can be seen in Figure 2.7, where the red angle represents the yaw angle and the green angle represents the pitch angle. The origin is representing the LV's bottom center where the nozzle is attached to the body, also known as the pivot point, P_{PVP} [1].

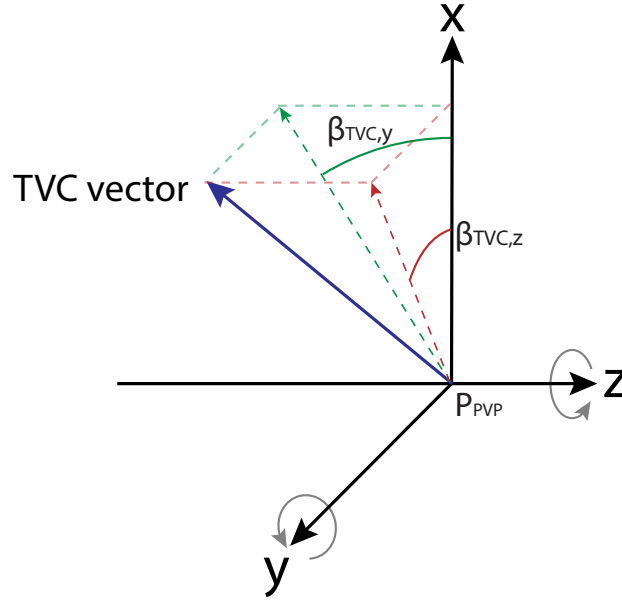


Figure 2.7: Visualization of the angles of the movable nozzle affects the TVC direction [1].

The force from the TVC in the BF reference frame can be deduced by first computing the direction force of the main engine thruster:

$$F_{TVC,T} = F_{TVC}(t) \begin{bmatrix} 1 \\ 0 \\ 0 \end{bmatrix} \quad (2.22)$$

where $F_{TVC}(t)$ is the thrust force from the main engine and is assumed not to be controllable since a full thrust is desirable for minimizing time in the atmosphere. The vector is to indicate that the thrust from the main engine, is only applying thrust in its own longitudinal direction. In other words, $F_{TVC,T}(t)$ is defined in the reference frame relative to the thruster itself. By knowing the thruster nozzle can move in two directions, $\{\beta_{TVC,y}, \beta_{TVC,z}\}$, the rotational DCMs Equation 2.2 and Equation 2.3 derived back in Section 2.3 can be utilized to transform $F_{TVC,T}(t)$ into the BF frame. This relationship can be seen in Equation 2.23:

$$\begin{aligned} F_{TVC,B}(t) &= C_z C_y F_{TVC,T} \\ &= F_{TVC}(t) \begin{bmatrix} \cos \beta_{TVC,y}(t) \cos \beta_{TVC,z}(t) \\ -\cos \beta_{TVC,y}(t) \sin \beta_{TVC,z}(t) \\ -\sin \beta_{TVC,y}(t) \end{bmatrix} \end{aligned} \quad (2.23)$$

Furthermore, the moment around the CG of the LV in the BF frame is given by Equation 2.24.

$$M_{TVC,B}(t) = (P_{PVP} - P_{CG}(t)) \times F_{TVC,B}(t) \quad (2.24)$$

Thrust data of $F_{TVC}(t)$ is provided by ESA and can be seen in Figure 2.8.

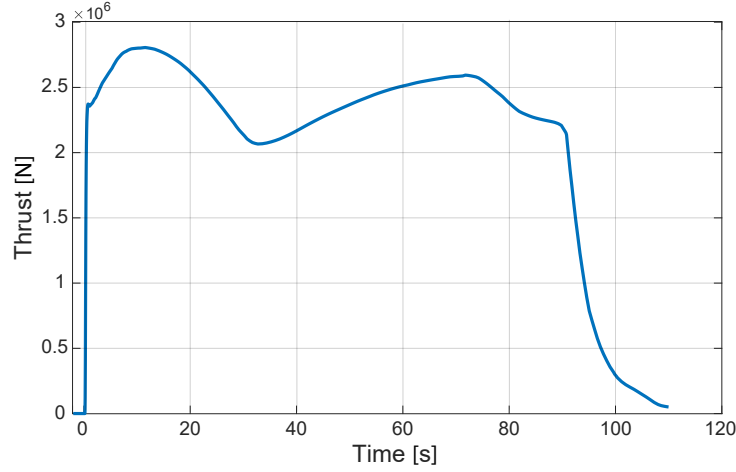


Figure 2.8: TVC thrust force data provided by ESA

This section has covered the deduction of the TVC force and momentum. The next section will describe and evaluate the nozzle itself.

2.7 Nozzle Dynamics

This section describes the nozzle dynamics also known as Tail-Wags-Dog (TWD) effect. Intuitively, when the nozzle needs to gimbal, the TVC system creates a force on the nozzle to make it move. This force on the nozzle creates a force back onto the LV and creates the TWD phenomenon.

The acceleration from when an engine gimbals creates inertia forces and torques. This effect is essential to model, not only for the rigid-body motion but also for the flexible-body motion described in the next section.

The nozzle dynamics in BF reference frame are given by:

$$F_{N,B} = -m_N l_N \ddot{\beta} \quad (2.25)$$

$$M_{N,B} = -(m_N l_N l_{CG} + J_N) \ddot{\beta} \quad (2.26)$$

where:

$\ddot{\beta}$	is the acceleration of the nozzle actuator.	[deg/s ²]
m_N	is the mass of the LV nozzle.	[kg]
l_N	is the distance from the nozzle center of gravity to P_{PVP} .	[m]
J_N	is the moment of inertia of the nozzle engine about P_{PVP} .	[kg · m ²]

The parameters have been provided by ESA:
 $m_N = 1616 \text{ kg}$, $l_N = 0.66 \text{ m}$ and $J_N = 1263.4 \text{ kg/m}^2$.

2.8 Flexible-Body Dynamics

In the previous sections, it was assumed that the vehicle behaved as a rigid body. However, in the response to various loads, the vehicle fuselage slightly bends elastically out of shape. The shape depends on time and bends in and out of shape at a particular frequency. This means that a certain shape of the beam can be predicted, this is also known as a bending mode [24].

The particular frequency corresponds with the natural frequency of the LV. An LV has in practice a combination of several bending modes, where each bending mode successively has a certain higher frequency. Bending modes can be set in motion by wind gusts or turbulence with similar frequency of that of the natural frequency of the LV. Successively higher bending modes have successively lower amplitude [24]. In practice, this means that a sufficient approximation can be made by only modelling a limited number of bending modes, since the effect from the higher frequency bending modes will become negligible.

The fuselage classifies as a free-free beam which means the ends are unrestrained. This classification influences how the bending modes are shaped. In Figure 2.9A, the first two bending modes of a uniform free-free beam are shown. The blue beam represents the first bending mode and the green beam represents the second bending mode. Figure 2.9B illustrates how the same two bending modes are affecting the LV, where the blue and green beam are added together and the resulting bending mode is represented with the red color. Note that in a real scenario, mass and aerodynamic forces are distributed non-uniformly along the fuselage, thus resulting in a different shape than the bending mode showed in Figure 2.9B.

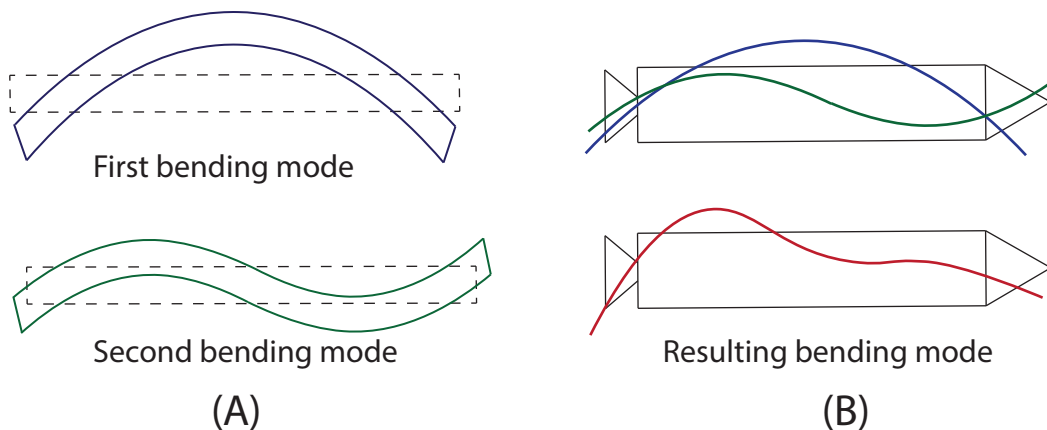


Figure 2.9: (A) Illustration of the two first bending modes in w.r.t. to a free free beam. (B) shows the two bending modes acting together on an LV.

In [23] a thorough modelling procedure of the flexible dynamics has been carried out. The general dynamical behavior of the i^{th} bending mode can be represented by the following 2^{nd} order model:

$$\ddot{q}_i + 2\zeta_{q_i}\omega_{q_i}\dot{q}_i + \omega_{q_i}^2 q_i = \frac{\int_0^L F_{total}(t) dL}{\int_0^L m(t) dL} \quad (2.27)$$

where:

q_i	is the state of the i^{th} bending mode.	$[m]$
ζ_{q_i}	is the dampening ratio of the i^{th} bending mode.	$[\cdot]$
ω_{q_i}	is the natural frequency of the i^{th} bending mode.	$[\text{rad}]$
$F_{total}(t)$	is the total translational force.	$[N]$
$m(t)$	is the mass of the vehicle.	$[\text{kg}]$
L	is the length of the vehicle.	$[m]$

The reason for integrating is to evaluate for the practical non-uniform distribution of forces and mass.

According to [23], the most dominant terms for the flexible dynamics are the thrust deflection and engine inertia. These are sufficient for purposes of a simplified analysis [19] [25] [22] [24] [26]. For the simplified analysis, the total force are expressed in Equation 2.28 [19] [25]:

$$\int_0^L F_{total}(t) dL = -F_{TVC,ref}(t)\Psi_t^{PVP_i}\beta_{TVC} - (m_N l_N \Psi_t^{PVP_i} - I_N \Psi_r^{PVP_i})\ddot{\beta}_{TVC} \quad (2.28)$$

where:

$\Psi_t^{PVP_i}$	is the translational length of the i^{th} bending mode at P_{PVP} .	$[m]$
$\Psi_r^{PVP_i}$	is the rotational angle of the i^{th} bending mode at P_{PVP} .	$[\text{rad}]$

The mass of the vehicle in Equation 2.27 can be omitted since the mode shapes $\Psi_t^{PVP_i}$ and $\Psi_r^{PVP_i}$ are already normalized with respect to the mass [25]. Additionally, β_{TVC} represents either a pitch or a yaw gimbal angle of the nozzle.

In Figure 2.10 is an illustration showing how the flexible terms, $\Psi_t^{PVP_i}$ and $\Psi_r^{PVP_i}$, are affecting the thrust deflection in the pitch plane w.r.t. the first bending mode. The black dot represents the LV's rigid-body pivot point and, as with the previous figure, the blue color is representing the first bending mode. In the figure the rigid-body pivot point is bent towards the blue pivot point. As a consequence the lateral displacement $\Psi_t^{PVP_i}$ and angle displacement $\Psi_r^{PVP_i}$ occurs.

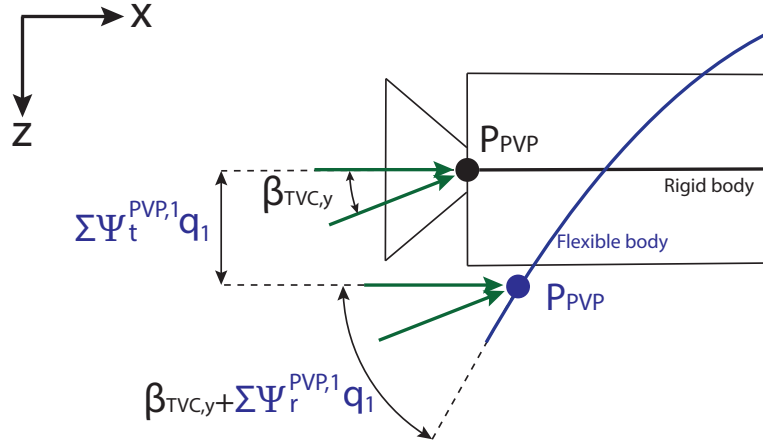


Figure 2.10: Flexible body diagram of how the first bending mode is affecting the thrust deflection

The bending modes add a local rotation and additional transitional force to the commanded gimbal angle β_{TVC} . In the BF reference frame, both the flexible-body motion force and moments considering k bending modes are expressed by Equation 2.29 and Equation 2.30, respectively [19].

$$F_{F,B}(t) = F_{TVC,ref} \sum_{i=1}^k \Psi_r^{PVP_i} q_i \quad (2.29)$$

$$M_{F,B}(t) = -F_{TVC,ref} \left(\sum_{i=1}^k \Psi_r^{PVP_i} q_i + \sum_{i=1}^k \Psi_t^{PVP_i} q_i \right) \quad (2.30)$$

In this project, there will be modelled two bending modes. This is because the frequency of the third bending mode is already higher than the Nyquist frequency of the VEGA LV according to ESA. This makes modelling of bending modes beyond two irrelevant since they cannot be processed. All the parameters described in this section are model-specific and ESA has provided all the required values.

The parameters are varying with time due to the changing dynamics throughout the flight. They are partitioned like so: $[x_{t=0} \quad x_{t=end}]$, where $x_{t=0}$ is the value of the given parameter at liftoff and $x_{t=end}$ is the parameter value at MECO.

$$\begin{aligned} \Psi_t^{PVP_1} &= [3.67 \quad 9.02] 10^{-3} \text{ m}, & \Psi_t^{PVP_2} &= [2.26 \quad 3.57] 10^{-3} \text{ m} \\ \Psi_r^{PVP_1} &= [-0.94 \quad -1.55] 10^{-3} \text{ rad}, & \Psi_r^{PVP_2} &= [-0.97 \quad -1.76] 10^{-3} \text{ rad} \\ \omega_{q1} &= [25.51 \quad 37.01] \text{ rad}, & \omega_{q2} &= [66.98 \quad 84.57] \text{ rad} \\ \zeta &= 0.008 \end{aligned}$$

In the project, the minimum and maximum values will be affinely interpolated between as many times as there are data points in the simulation from [1].

The next section is describing how the bending modes are affecting the sensor measurements.

2.9 Sensor Characterization

The sensors measure the position, velocity, rotation and angular velocity of the LV. In order to model the output matrix, a definition of the position and orientation of the LV and its velocities at the location of where the sensors are mounted is defined.

Back in Section 2.3 the DCM $C_{I \rightarrow B}$ was derived in Equation 2.4. By applying the DCM on the coordinate of where the sensor is mounted on the LV, the angle w.r.t the sensor can be defined. Together with the position of the LV's CG, the exact position and orientation can be found. This is described in Equation 2.31.

$$\begin{aligned} r_{INS,rigid} &= \begin{bmatrix} r_x \\ r_y \\ r_z \end{bmatrix} + C_{I \rightarrow B} [P_{INS} - P_{CG}] \\ &= \begin{bmatrix} r_x - \cos(\theta_y) \cos(\theta_z) (P_{CG} - P_{INS}) \\ r_y + \cos(\theta_y) \sin(\theta_z) (P_{CG} - P_{INS}) \\ r_z + \sin(\theta_y) (P_{CG} - P_{INS}) \end{bmatrix} \end{aligned} \quad (2.31)$$

where INS was introduced back in Section 2.1 on page 6 and P_{INS} is the location of the sensor on the body of the LV.

The motions at the sensor location can be described by the velocity vector and the angular velocity vector:

$$\begin{aligned} \dot{r}_{INS,rigid} &= \begin{bmatrix} \dot{r}_x \\ \dot{r}_y \\ \dot{r}_z \end{bmatrix} + \begin{bmatrix} \dot{\theta}_x \\ \dot{\theta}_y \\ \dot{\theta}_z \end{bmatrix} \times (P_{INS} - P_{CG}) \\ &= \begin{bmatrix} \dot{r}_x \\ \dot{r}_y - \dot{\theta}_z (P_{CG} - P_{INS}) \\ \dot{r}_z + \dot{\theta}_y (P_{CG} - P_{INS}) \end{bmatrix} \end{aligned} \quad (2.32)$$

Since the flexible dynamics, from the previous section, are causing the fuselage to bend, the measurements from the sensors located on the LV are influenced. The measured attitude, drift and their derivatives are given by [19]:

$$\theta_{INS} = \theta - \sum_{i=1}^k \Psi_r^{INS_i} q_i \quad (2.33)$$

$$\dot{\theta}_{INS} = \dot{\theta} - \sum_{i=1}^k \Psi_r^{INS_i} \dot{q}_i \quad (2.34)$$

$$r_{INS} = r - l_{INS} \theta + \sum_{i=1}^k \Psi_t^{INS_i} q_i \quad (2.35)$$

$$\dot{r}_{INS} = \dot{r} - l_{INS}\dot{\theta} + \sum_{i=1}^k \Psi_t^{INS_i} \dot{q}_i \quad (2.36)$$

where:

$\Psi_t^{INS_i}$	is the translational length of the i^{th} bending mode at P_{INS} .	[m]
$\Psi_r^{INS_i}$	is the rotational angle of the i^{th} bending mode at P_{INS} .	[rad]
θ	is the angle vector $[\theta_x \ \theta_y \ \theta_z]^T$	[rad]
$\dot{\theta}$	is the angle velocity vector $[\dot{\theta}_x \ \dot{\theta}_y \ \dot{\theta}_z]^T$	[rad/s]
r	is the position vector $[x \ y \ z]^T$	[m]
\dot{r}	is the velocity vector $[\dot{r}_x \ \dot{r}_y \ \dot{r}_z]^T$	[m/s]
l_{INS}	is the distance between P_{INS} and P_{CG}	[m]

Below is the parameter data provided by ESA and partitioned like the previous section: $[x_{t=0} \ x_{t=end}]$, where $x_{t=0}$ is the value of the given parameter at the start of the flight and $x_{t=end}$ is the parameter value at MECO. P_{INS} is partitioned with coordinates: $[x_{INS} \ y_{INS} \ z_{INS}]$.

$$\begin{aligned} \Psi_t^{INS_1} &= [10.22 \ 10.26] 10^{-3} \text{ m}, & \Psi_t^{INS_2} &= [-6.13 \ -5.46] 10^{-3} \text{ m} \\ \Psi_r^{INS_1} &= [1.95 \ 2.27] 10^{-3} \text{ rad}, & \Psi_r^{INS_2} &= [-2.25 \ -2.51] 10^{-3} \text{ rad} \\ P_{INS} &= [22.9 \ 0 \ 0] \text{ m} \end{aligned}$$

The bending modes are also affinely interpolated between for each time step in the simulation.

Summary

Finally, all the necessary characteristics for the VEGA LV have been deduced and evaluated in the last several sections. The gravitational force and momentum has not been necessary to evaluate, which will come clear why in subsection 2.10.1. The next section will describe how the LV model will be linearized.

2.10 Model Linearization

This section will be covering the method of linearization. Since the launch vehicle is assumed to be operating in a highly non-linear environment, the LV will be linearized at several time instances along its trajectory. Eventually, the idea is to design a family of linear controllers from the LV's respective state space representations and apply them at the appropriate operational points. This gain scheduling methodology is a standard practice to deal with systems with a wide dynamic variation and is also used in control of LVs [19].

According to [23] and [8], a way to simplify the model substantially without losing too much accuracy, is to only include the pitch plane and not focus on the yaw plane. This is possible with the assumption that the LV is axisymmetric around its longitudinal axis. That way, the pitch and yaw motions can be assumed uncoupled and the task of attitude

control can be performed in a single plane. In this thesis, only the pitch plane will be analyzed.

The non-linear dynamics consist of the aerodynamical, TVC and sensor characteristics covered in Section 2.5, Section 2.6 and Section 2.9, respectively. These dynamics will be linearized with Jacobian linearization, where for each equation, a first order partial derivative w.r.t. either a state or a control signal is evaluated.

The method that was conducted in this thesis, was to solve the Jacobian first and then inserting operating points corresponding to a point on the trajectory where it was desired to linearize. This method provided more efficiency computational-wise since the Jacobian was only required to be solved once, when linearizing at several time instances. Later in subsection 2.10.1 the operating points are covered.

The general formula for the Jacobian is given in Equation 2.37.

$$J = \begin{bmatrix} \frac{\partial f_1}{\partial x_1} & \dots & \frac{\partial f_1}{\partial x_n} \\ \vdots & \ddots & \vdots \\ \frac{\partial f_m}{\partial x_1} & \dots & \frac{\partial f_m}{\partial x_n} \end{bmatrix} \quad (2.37)$$

Below are the Jacobians split up in states and control variables since none of the control dynamics are dependent on the aerodynamic forces and vice versa. The Jacobian from the aerodynamic equations can be seen in Equation 2.38 and the Jacobian from the control signals can be seen in Equation 2.39. Note that due to readability θ_y , r_z , $\beta_{TVC,y}$, $v_{w,z}$ and $Q_{\alpha,total}$ will now simply be denoted θ , z , β_{TVC} , v_w and Q_α , respectively.

$$J_A = \begin{bmatrix} \frac{\partial \ddot{\theta}_{aero,B}}{\partial \theta} & \frac{\partial \ddot{\theta}_{aero,B}}{\partial \theta} & \frac{\partial \ddot{\theta}_{aero,B}}{\partial z} & \frac{\partial \ddot{\theta}_{aero,B}}{\partial \dot{z}} \\ \frac{\partial \ddot{r}_{aero,B}}{\partial \theta} & \frac{\partial \ddot{r}_{aero,B}}{\partial \theta} & \frac{\partial \ddot{r}_{aero,B}}{\partial z} & \frac{\partial \ddot{r}_{aero,B}}{\partial \dot{z}} \end{bmatrix} \quad (2.38)$$

$$J_B = \begin{bmatrix} \frac{\partial \ddot{\theta}_{TVC,B}}{\partial \beta_{TVC}} \\ \frac{\partial \ddot{r}_{TVC,B}}{\partial \beta_{TVC}} \end{bmatrix} \quad (2.39)$$

where J_A represents the Jacobian for the dynamics of the LV and J_B represents the Jacobian for the control signals.

The disturbances are also linearized with a Jacobian but w.r.t. to the wind velocity $v_w(t)$:

$$J_{Bd} = \begin{bmatrix} \frac{\partial \ddot{\theta}_{TVC,B}}{\partial v_w} \\ \frac{\partial \ddot{r}_{TVC,B}}{\partial v_w} \end{bmatrix} \quad (2.40)$$

The first entry in the output matrix will be the performance indicator Q_α introduced back in Section 2.5. The following entries will be the states of the system and so the Jacobian will follow the structure:

$$J_C = \begin{bmatrix} \frac{\partial \dot{Q}_\alpha}{\partial \theta} & \frac{\partial \dot{Q}_\alpha}{\partial \dot{\theta}} & \frac{\partial \dot{Q}_\alpha}{\partial z} & \frac{\partial \dot{Q}_\alpha}{\partial \dot{z}} \\ \frac{\partial \ddot{\theta}_{aero,B}}{\partial \theta} & \frac{\partial \ddot{\theta}_{aero,B}}{\partial \dot{\theta}} & \frac{\partial \ddot{\theta}_{aero,B}}{\partial z} & \frac{\partial \ddot{\theta}_{aero,B}}{\partial \dot{z}} \\ \frac{\partial \ddot{r}_{aero,B}}{\partial \theta} & \frac{\partial \ddot{r}_{aero,B}}{\partial \dot{\theta}} & \frac{\partial \ddot{r}_{aero,B}}{\partial z} & \frac{\partial \ddot{r}_{aero,B}}{\partial \dot{z}} \end{bmatrix} \quad (2.41)$$

The Jacobian for the direct control method is not needed, since there are no equations dependent on the control signal β_{TVC} directly, $J_D = [0_{5,1}]$.

The Jacobian for the direct disturbance are, like the control disturbances, evaluated for w.r.t. v_w :

$$J_{Dd} = \begin{bmatrix} \frac{\partial \dot{Q}_\alpha}{\partial v_w} \\ \frac{\partial \ddot{\theta}_{TVC,B}}{\partial v_w} \\ \frac{\partial \ddot{r}_{TVC,B}}{\partial v_w} \end{bmatrix} \quad (2.42)$$

Now that the Jacobians have been described, the operating points are accounted for in the next section.

2.10.1 Operating Points

The operating points are chosen in the BF reference frame w.r.t. the gravity turn trajectory presented back in Figure 2.2 on page 8. From information about the gravity turn in Section 2.2, practical assumptions can be made. Recall that the gravity turn does not require any actuation efforts from the TVC system and the AoA is kept close to zero with the assumption that no wind disturbances are present. Additionally, gravity do not have to be considered, because the LV already follows a trajectory affected by it.

Table 2.2 shows the operating points used in this project. All the states are set to zero, since otherwise would mean a deviation from the reference trajectory. The nozzle gimbal is also set to zero because the LV is assumed to be in steady state [8]. The AoA is also set to zero and the wind disturbance is set to zero as a consequence of that. All the linearizations made throughout the atmospheric flight will be w.r.t. the gravity turn and thereby have these assumptions. Keep in mind that only the lateral position and velocity is set to zero. The longitudinal x-direction of the LV is still allowed to change.

Operating Points

θ_0	$\dot{\theta}_0$	z_0	\dot{z}_0	$\beta_{TVC,0}$	AoA ₀	$v_{w,0}$
0	0	0	0	0	0	0

Table 2.2: Table of operating points applicable for all linearizations made throughout the flight

The next section will partition the 2D LV model in a state space representation.

2.11 State Space Representation

This section will present a state space representation of the linearized equations of motion and sensor dynamics from the previous section.

The partitioning of the matrices in the state space representation is based on [25], where the rigid- and flexible-body contributions are expressed separately. The partitioning can be seen in Equation 2.43.

$$\begin{aligned} \begin{bmatrix} \dot{\mathbf{x}}_{\mathbf{R}} \\ \dot{\mathbf{x}}_{\mathbf{F}} \end{bmatrix} &= \begin{bmatrix} A_R & A_{RF} \\ A_{FR} & A_F \end{bmatrix} \begin{bmatrix} \mathbf{x}_{\mathbf{R}} \\ \mathbf{x}_{\mathbf{F}} \end{bmatrix} + \begin{bmatrix} B_R \\ B_F \end{bmatrix} \mathbf{u} + \begin{bmatrix} B_{d,R} \\ B_{d,F} \end{bmatrix} \mathbf{u}_d \\ \mathbf{y}_{\mathbf{LV}} &= \begin{bmatrix} C_R & C_F \end{bmatrix} \begin{bmatrix} \mathbf{x}_{\mathbf{R}} \\ \mathbf{x}_{\mathbf{F}} \end{bmatrix} + D_R \mathbf{u} + D_d \mathbf{u}_d \end{aligned} \quad (2.43)$$

where:

$$\begin{array}{l|l} A_R & \text{is the rigid-body dynamics.} \\ A_F & \text{is the flexible-body dynamics.} \\ A_{RF} & \text{is the coupled dynamics between the rigid body and flexible body.} \\ A_{FR} & \text{is the coupled dynamics between the flexible body and rigid body.} \end{array}$$

The LV system will be called G_{LV} and uses four rigid-body states, the pitch attitude angle θ , the lateral drift z and their respective derivatives: $\mathbf{x}_{\mathbf{R}} = [\theta \ \dot{\theta} \ z \ \dot{z}]^T$. There are also four flexible-body states, a state q and its derivative for the two first bending modes $\mathbf{x}_{\mathbf{F}} = [q_1 \ q_2 \ \dot{q}_1 \ \dot{q}_2]^T$. There are five outputs $\mathbf{y}_{\mathbf{LV}} = [Q_\alpha \ \theta_{INS} \ \dot{\theta}_{INS} \ z_{INS} \ \dot{z}_{INS}]^T$. Here the performance indicator Q_α is included in the first entry. Recall that back in Section 2.5 this performance indicator is of interest, since it evaluates the impact of trajectory and attitude on induced loads on the LV. $\theta_{INS}, \dot{\theta}_{INS}, z_{INS}$ and \dot{z}_{INS} are all measurements from sensors.

G_{LV} will have three inputs $\mathbf{u} = [\beta_{TVC} \ \ddot{\beta}_{TVC}]^T$ and $\mathbf{u}_d = v_w$. Here the acceleration of the nozzle deflection $\ddot{\beta}_{TVC}$ is considered as an input to account for the TWD effect [19].

The matrices of the state space are given as in Equation 2.44 on the next page:

$$\begin{aligned}
 & \begin{bmatrix} \dot{\theta} \\ \ddot{\theta} \\ \dot{z} \\ \ddot{z} \\ \dot{q}_1 \\ \dot{q}_2 \\ \ddot{q}_1 \\ \ddot{q}_2 \end{bmatrix} = \begin{bmatrix} 0 & 1 & 0 & 0 & 0 & 0 & 0 & 0 \\ a_{\ddot{\theta}\theta} & a_{\ddot{\theta}\dot{\theta}} & 0 & a_{\ddot{\theta}z} & a_{\ddot{\theta}q_1} & a_{\ddot{\theta}q_2} & 0 & 0 \\ 0 & 0 & 0 & 1 & 0 & 0 & 0 & 0 \\ a_{\ddot{z}\theta} & a_{\ddot{z}\dot{\theta}} & 0 & a_{\ddot{z}z} & a_{\ddot{z}q_1} & a_{\ddot{z}q_2} & 0 & 0 \\ 0 & 0 & 0 & 0 & 0 & 0 & 1 & 0 \\ 0 & 0 & 0 & 0 & 0 & 0 & 0 & 1 \\ 0 & 0 & 0 & 0 & a_{\ddot{q}_1q_1} & 0 & a_{\ddot{q}_1q_2} & 0 \\ 0 & 0 & 0 & 0 & 0 & a_{\ddot{q}_2q_2} & 0 & a_{\ddot{q}_2q_1} \end{bmatrix} \begin{bmatrix} \theta \\ \dot{\theta} \\ z \\ \dot{z} \\ q_1 \\ q_2 \\ \dot{q}_1 \\ \dot{q}_2 \end{bmatrix} \\
 & + \begin{bmatrix} 0 & 0 \\ b_{\ddot{\theta}\beta} & b_{\ddot{\theta}\ddot{\beta}} \\ 0 & 0 \\ b_{\ddot{z}\beta} & b_{\ddot{z}\ddot{\beta}} \\ 0 & 0 \\ 0 & 0 \\ b_{\ddot{q}_1\beta} & b_{\ddot{q}_1\ddot{\beta}} \\ b_{\ddot{q}_2\beta} & b_{\ddot{q}_2\ddot{\beta}} \end{bmatrix} \begin{bmatrix} \beta_y \\ \ddot{\beta}_y \end{bmatrix} + \begin{bmatrix} 0 \\ 0 \\ 0 \\ 0 \\ 0 \\ 0 \\ 0 \\ 0 \end{bmatrix} v_w \\
 & \begin{bmatrix} Q_\alpha \\ \theta_{INS} \\ \dot{\theta}_{INS} \\ z_{INS} \\ \dot{z}_{INS} \end{bmatrix} = \begin{bmatrix} Q & 0 & 0 & Q/V & 0 & 0 & 0 & 0 \\ 1 & 0 & 0 & 0 & \Psi_r^{INS1} & \Psi_r^{INS2} & 0 & 0 \\ 0 & 1 & 0 & 0 & 0 & 0 & \Psi_r^{INS1} & \Psi_r^{INS2} \\ x_{CG} - x_{INS} & 0 & 1 & 0 & \Psi_t^{INS1} & \Psi_t^{INS2} & 0 & 0 \\ 0 & x_{CG} - x_{INS} & 0 & 1 & 0 & 0 & \Psi_t^{INS1} & \Psi_t^{INS2} \end{bmatrix} \begin{bmatrix} \theta \\ \dot{\theta} \\ z \\ \dot{z} \\ q_1 \\ q_2 \\ \dot{q}_1 \\ \dot{q}_2 \end{bmatrix} \\
 & + \begin{bmatrix} 0 & 0 \\ 0 & 0 \\ 0 & 0 \\ 0 & 0 \\ 0 & 0 \end{bmatrix} \begin{bmatrix} \beta_{TVC} \\ \ddot{\beta}_{TVC} \end{bmatrix} + \begin{bmatrix} -Q/V \\ 0 \\ 0 \\ 0 \\ 0 \end{bmatrix} v_w \tag{2.44}
 \end{aligned}$$

where:

$$\begin{aligned}
 b_{\ddot{\theta}\beta} &= -\frac{F_{TVC}(x_{CG}-x_{PVP})}{J_y} & b_{\ddot{q}_1\beta} &= -\Psi_t^{PVP1} F_{TVC} \\
 b_{\ddot{z}\beta} &= -\frac{F_{TVC}}{m} & b_{\ddot{q}_2\beta} &= -\Psi_t^{PVP2} F_{TVC} \\
 b_{\ddot{\theta}\ddot{\beta}} &= -\frac{J_{ny}+m_n l_n (x_{CG}-x_{PVP})}{J_y} & b_{\ddot{q}_1\ddot{\beta}} &= J_{ny} \Psi_r^{PVP1} - \Psi_t^{PVP1} m_n l_n \\
 b_{\ddot{z}\ddot{\beta}} &= -\frac{m_n l_n}{m} & b_{\ddot{q}_2\ddot{\beta}} &= J_{ny} \Psi_r^{PVP2} - \Psi_t^{PVP2} m_n l_n
 \end{aligned}$$

$$\begin{aligned}
 a_{\ddot{q}_1q_1} &= -\omega_{q1}^2 & a_{\dot{\theta}q_1} &= \frac{F_{TVC}(\Psi_t^{PVP1} + \Psi_r^{PVP1}(x_{CG}-x_{PVP}))}{J_y} - \\
 a_{\ddot{q}_2q_2} &= -\omega_{q2}^2 & a_{\dot{\theta}q_2} &= \frac{-F_{TVC}(\Psi_t^{PVP2} + \Psi_r^{PVP2}(x_{CG}-x_{PVP}))}{J_y} \\
 a_{\ddot{q}_1q_1} &= -2\omega_{q1} \zeta & a_{zq_1} &= \frac{\Psi_r^{PVP1} F_{TVC}}{m} \\
 a_{\ddot{q}_2q_2} &= -2\omega_{q2} \zeta & a_{zq_2} &= \frac{\Psi_r^{PVP2} F_{TVC}}{m}
 \end{aligned}$$

$$\begin{aligned}
a_{\ddot{\theta}\theta} &= -\frac{S_{\text{ref}} \rho_{\text{air}} \sigma_1 v_x^2 (x_{\text{CG}} - x_{\text{CP}})}{2 J_y} \\
a_{\dot{\theta}\dot{\theta}} &= \frac{S_{\text{ref}} \rho_{\text{air}} \sigma_1 v_x (x_{\text{CG}} - x_{\text{CP}})^2}{2 J_y} \\
a_{\ddot{\theta}z} &= -\frac{S_{\text{ref}} \rho_{\text{air}} \sigma_1 v_x (x_{\text{CG}} - x_{\text{CP}})}{2 J_y} \\
a_{z\ddot{\theta}} &= \frac{S_{\text{ref}} \rho_{\text{air}} \sigma_1 v_x^2}{2 m} \\
a_{z\dot{\theta}} &= -\frac{S_{\text{ref}} \rho_{\text{air}} \sigma_1 v_x (x_{\text{CG}} - x_{\text{CP}})}{2 m} \\
a_{z\ddot{z}} &= \frac{S_{\text{ref}} \rho_{\text{air}} \sigma_1 v_x}{2 m}
\end{aligned}$$

where

$$\sigma_1 = \frac{\partial C_N}{\partial \alpha} = \frac{\partial (C_L \cos \alpha + C_D \sin \alpha)}{\partial \alpha}$$

For analysis and design purposes, the nominal state space system G_{LV} is used to derive nominal LTI models at different operating points along the gravity turn trajectory with the assumption that the parameters are frozen in time. The nominal frequency responses at different time instants are plotted in Figure 2.11A on the next page. From the frequency response it can be seen that the magnitude changes during the atmospheric flight. This can clearly be seen throughout the whole frequency range. This plot also shows the frequency for each bending mode peak increases with time.

On Figure 2.11B the poles and zeros of G_{LV} can be seen. The launcher has eight poles in total, four from the rigid-body dynamics and four from the flexible-body dynamics, two for each bending mode. The control stabilization problem lies mainly in stabilizing the dynamics, which are dependent on the velocity squared, recall coefficient $a_{\ddot{\theta}\theta}$, $a_{z\ddot{\theta}}$ and the relation: $Q = 0.5 \rho_{\text{air}} V^2$. The dynamic pressure is at its highest at around 50 - 60 seconds into the atmospheric flight, which is where it can be seen the poles are most unstable. Besides the stabilization, the performance can also be challenging around this part of the ascent. At this part, it requires more control actuation in order to counteract the torque generated by structural loads. As with the translational poles, they require less control effort to stabilize due to their slow dynamical behavior [19].

Now that the state space representation of the LV (G_{LV}) has been established and analyzed, uncertainties in the model will be evaluated for in the next section.

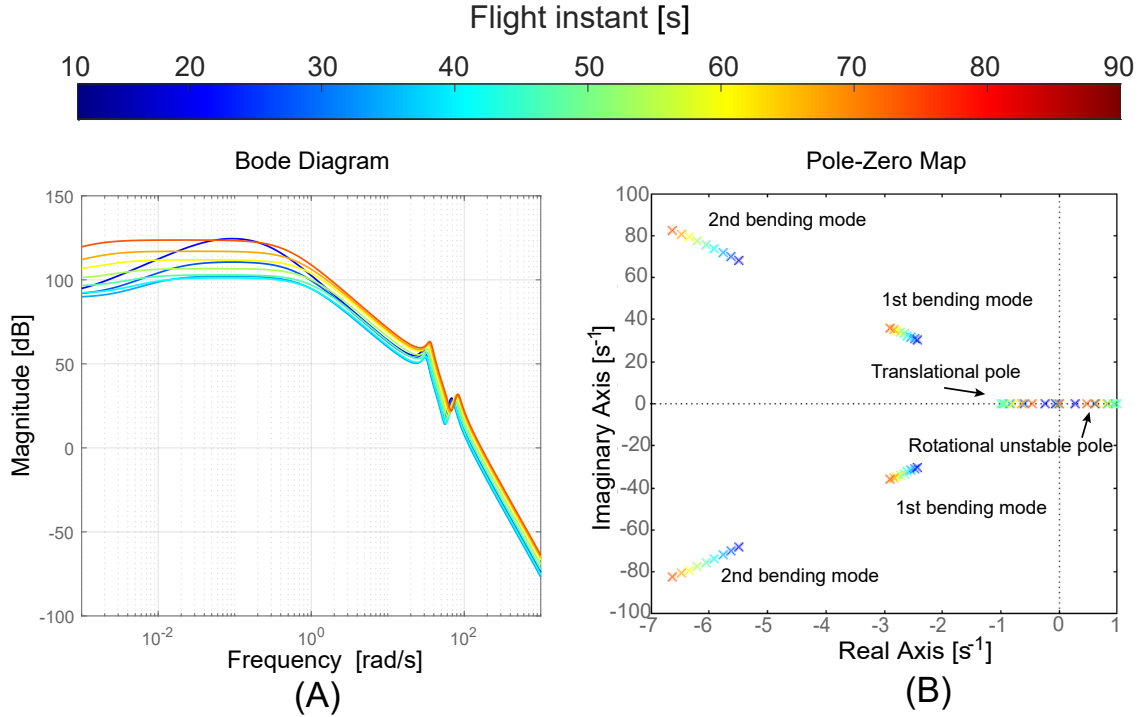


Figure 2.11: (A) showing the attitude frequency response ($\theta_{\text{INS}}(\omega)/\beta_{\text{TVC}}(\omega)$). (B) showing the pole-zero map of G_{LV} .

2.12 Uncertainty Modelling

Without robust control, a control system is designed to work with a single nominal plant model. In some cases, this system can be sufficient for its respective application it is designed for. However, 100 % of the time the nominal plant model is not representing the actual plant. For any system the stability and performance are affected by many dynamical perturbations, that is uncertainties. These uncertainties come from external disturbances as well as modelling inaccuracies. A successful controller must function properly for all uncertainties within a bounded set [27].

This section begins with the necessary knowledge to integrate uncertainties into the model of the LV G_{LV} that was introduced in Equation 2.44 in the previous section. In this section, theory from [19] and [1] will be used to explain the Linear Fractional Transform (LFT) framework. This is followed by how the uncertainties are described in the model with a summary of all the relevant uncertain parameters for G_{LV} .

2.12.1 LFT Framework

G_{LV} can be augmented to incorporate uncertainties with LFT theory. The LFT is a known approach to model the known uncertainties of each parameter in a model. The LFT representation is used as a mathematical representation of the model of the LV and the known uncertainties defined by a state feedback interconnection between two matrices, $P \in \mathbb{C}^{(n_d+n_u) \times (n_e+n_y)}$ and $\Delta \in \mathbb{C}^{n_y \times n_u}$, where P is traditionally partitioned into four submatrices [19] [1]. This partitioning can be seen in Equation 2.45.

$$\begin{bmatrix} z \\ y \end{bmatrix} = P(s) \begin{bmatrix} w \\ u \end{bmatrix} = \begin{bmatrix} P_{11}(s) & P_{12}(s) \\ P_{21}(s) & P_{22}(s) \end{bmatrix} \begin{bmatrix} w \\ u \end{bmatrix} \quad (2.45)$$

where:

u	is the control variables.
y	is the measured variables.
w	is the exogenous signals such as disturbances and commands.
z	is the so-called error signals which are to be minimized in some sense to meet the control objectives.

The two types of LFT interconnections are shown in Figure 2.12. Where (A) is showing the upper LFT interconnection and (B) is showing the lower LFT interconnection.

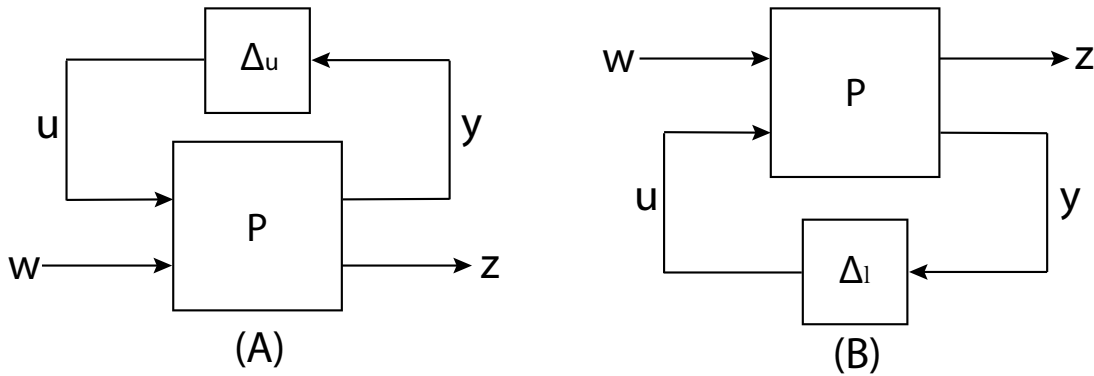


Figure 2.12: (A) showing the upper LFT interconnection and (B) showing the lower LFT interconnection [1]

Here the upper LFT describes the relation between the nominal plant P and the known uncertainties Δu . The \mathcal{F}_u operator defines the closed loop from the input signal w to the output signal z . The definition can be seen in Equation 2.46.

$$\mathcal{F}_u(P, \Delta u) = P_{22} + P_{21}\Delta u(I - P_{11})^{-1}P_{12} \quad (2.46)$$

This representation is often used to model uncertainties in robust control theory. It can be used to model plants subject to uncertainties through Δu , where Δu is a block-diagonal transfer matrix including all possible perturbations.

Furthermore, the lower LFT interconnection is describing the relation between P and Δl through the operator \mathcal{F}_l . This relation can be seen in Equation 2.47.

$$\mathcal{F}_l(P, \Delta l) = P_{11} + P_{12}\Delta l(I - P_{22})^{-1}P_{21} \quad (2.47)$$

The lower LFT form will later be used in Chapter 4 for synthesizing a controller for the LV system.

As an example for defining an uncertain parameter, assume that a given parameter x has an uncertainty range σ_x around its nominal value. This is modelled as an input multiplicative perturbation through the variation around its nominal value. This is also represented in Equation 2.48.

$$x = x^0(1 + \sigma_x\delta_x), \quad \delta_x \in [-1 \ 1] \quad (2.48)$$

where δ_x is a bounded uncertainty flag.

With Equation 2.46 in mind, this effect can also be written on LFT form by having in the nominal system set to:

$$P = \begin{bmatrix} 0 & 1 \\ x^0\sigma_x & x^0 \end{bmatrix} \quad (2.49)$$

Every time the uncertain parameter x appears in a linear time-invariant system, it can be replaced by Figure 2.13 [27].

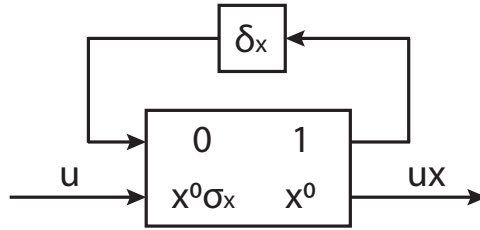


Figure 2.13: LFT representation of an arbitrary uncertain parameter x

2.12.2 Uncertain LV Model

In Table 2.3 on the next page are all the uncertain parameters' respective nominal values and uncertainties are listed. The nominal values are imported from the simulation explained back in subsection 1.3.1 and the uncertainties have been provided by ESA. The parameters are split up in rigid-body parameters and flexible-body parameters. All the values have been gathered from fifty seconds into the flight, as this is where the maximum dynamic pressure will be at its highest and therefore corresponds to where the uncertainties are considered to be most severe [19].

Variable	Symbol	Units	Nominal	Uncertainty
Thrust force	F_{TVC}	kN	2510.6	10 %
Longit. velocity	v_x	m/s	834.6	10 %
Air density	ρ_{air}	Pa	0.1323	10 %
Longit. CP coordinate	x_{CP}	m	29.8	10 %
Longit. CG coordinate	x_{CG}	m	9.4	2 %
Total RLV mass	m	kg	79275	2 %
Pitch inertia	J_y	kg · m ²	46 · 10 ⁵	2 %
1st natural freq.	ω_{q1}	rad	5.4132	[-20 15]%
2nd natural freq.	ω_{q2}	rad	12.3287	[-25 20]%
1st PVP trans. length	Ψ_t^{PVP1}	m	0.0069	[-40 30]%
2nd PVP trans. length	Ψ_t^{PVP2}	m	-0.0057	50 %
1st PVP rot. angle	Ψ_r^{PVP1}	rad	-0.0013	[-40 30]%
2nd PVP rot. angle	Ψ_r^{PVP2}	rad	-0.0014	50 %
1st INS trans. length	Ψ_t^{INS1}	m	0.0102	[-40 30]%
2nd INS trans. length	Ψ_t^{INS2}	m	-0.0057	50 %
1st INS rot. angle	Ψ_r^{INS1}	rad	0.0021	[-40 30]%
2nd INS rot. angle	Ψ_r^{INS2}	rad	-0.0024	50 %

Table 2.3: Table showing all the parameters' nominal values and uncertainties. The parameters are split up in rigid-body parameters and flexible-body parameters [8]

All the parametric uncertainties introduced in Table 2.3 are presented in a similar way as in Figure 2.13. Here the uncertainty block is partitioned as a diagonal matrix with all the uncertainty flags from the rigid-body dynamics listed first followed by the flexible-body dynamics: $\Delta_{LV} = \text{diag}(\Delta_{LV,R}, \Delta_{LV,F})$. Δ_{LV} represents the Δ_u -block shown back in Figure 2.12A and $\Delta_{LV,R}$ and $\Delta_{LV,F}$ are given in Equation 2.50 and Equation 2.51, respectively. I_\bullet is the identity matrix of size \bullet , where \bullet represents the number of times a given uncertain parameter is present in the state space representation. For example the uncertain parameter mass, m , occurs six times in Equation 2.44, hence I_\bullet will be a 6×6 identity matrix represented by the notation I_6 . In this thesis the parameters are defined using the Robust Control Toolbox provided by MATLAB [10]. The resulting VEGA LFT model has 87 dimensions when counting the parameters and their repetitions.

$$\Delta_{LV,R} = \text{diag} [I_{24}\delta v_x, I_{12}\delta x_{CG}, I_8\delta J_y, I_6\delta x_{CP}, I_6\delta m, I_6\delta \rho_{air}, I_3\delta T_{TVC}] \quad (2.50)$$

$$\Delta_{LV,F} = \text{diag} [I_2\delta \omega_{q1}, I_2\delta \omega_{q2}, I_3\delta \Psi_r^{PVP1}, I_3\delta \Psi_r^{PVP2}, I_2\delta \Psi_t^{PVP1}, I_2\delta \Psi_t^{PVP2}, I_2\delta \Psi_r^{INS1}, I_2\delta \Psi_r^{INS2}, I_2\delta \Psi_t^{INS1}, I_2\delta \Psi_t^{INS2}] \quad (2.51)$$

In Figure 2.14 the upper LFT representation of G_{LV} can be seen. Here the two commands β_{TVC} and $\dot{\beta}_{TVC}$ can be seen as input, $Q_\alpha, \theta_{INS}, \dot{\theta}_{INS}, z_{INS}, \dot{z}_{INS}$ can be seen as output and Δ_{LV} as the uncertainty block.

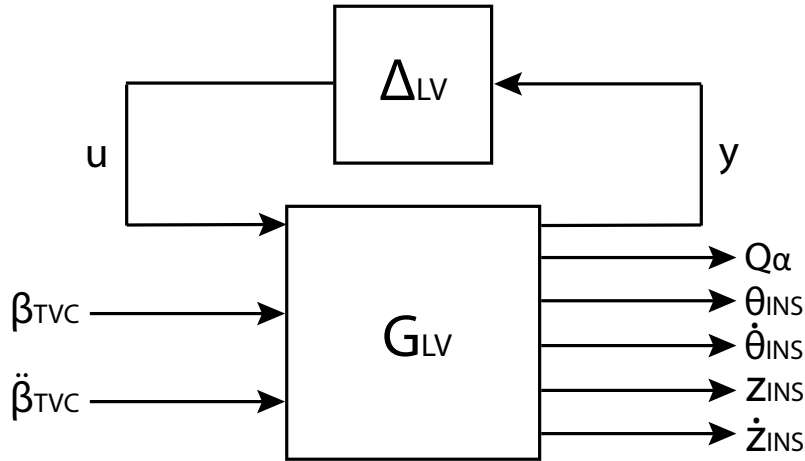


Figure 2.14: Upper LFT representation of G_{LV}

To illustrate the effect from the perturbations on the LV model, the frequency response at $t = 50$ s is plotted in Figure 2.15 with the nominal values represented by the red line and scattered responses in gray. Over the whole frequency range, this plot clearly shows the impact of uncertainties for the $\theta_{INS}(\omega)/\beta_{TVC}(\omega)$ channel. Note that each plot consists of random samples from the uncertainties and does not necessarily represent the worst-case response.

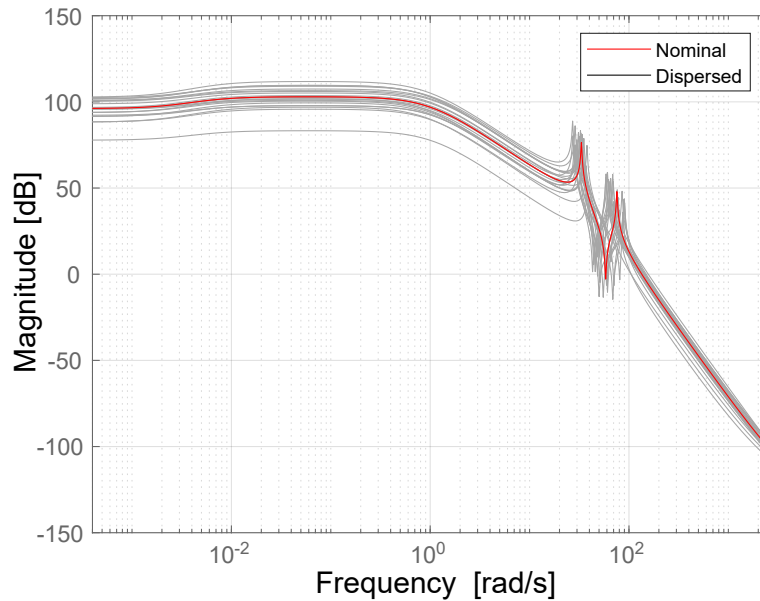


Figure 2.15: Bode plot of the upper LFT of $\theta_{INS}(\omega)/\beta_{TVC}(\omega)$ at 50 seconds

This section concludes the theory for the LV model, that has been present throughout the whole chapter. To conclude the chapter as a whole, a model for the TVC actuation system, a delay model and a wind disturbance model will be made in the next three subsections, respectively.

2.12.3 Uncertain TVC Actuation Model

The dynamics of the TVC actuators are characterized by the TVC actuator model. The model in this thesis is an approximation from [27] and [19]. There, the TVC actuator has been obtained from Hardware-In-the-Loop (HWIL) simulations. As with the LV model, the TVC actuator model is also described by an upper LFT configuration: $\mathcal{F}_u(G_{TVC}, \Delta_{TVC})$, where there has been given an uncertainty on 10 % on its dynamics. The nominal frequency response together with the dispersed response can be seen in Figure 2.16. Additionally, the upper LFT configuration for the TVC actuation model can be seen in Figure 2.17B.

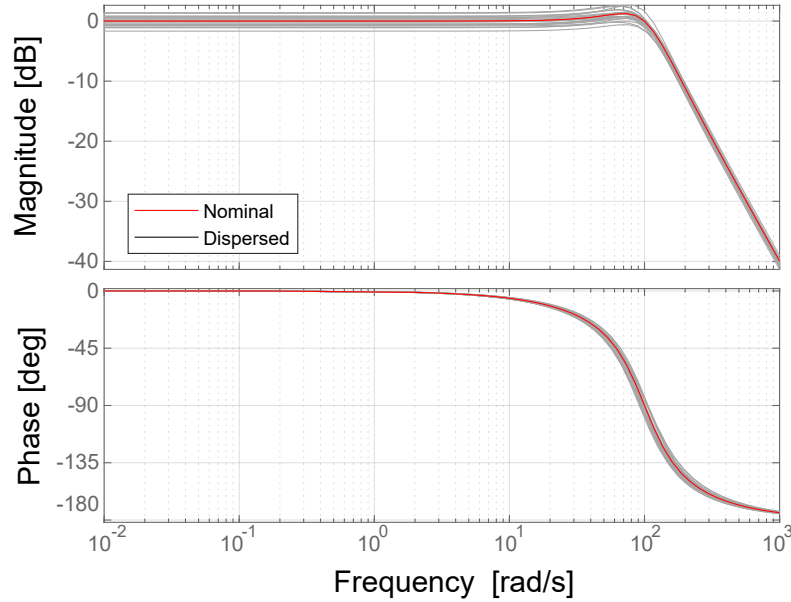


Figure 2.16: Frequency response the TVC model

2.12.4 Uncertain Delay Model

Delays in the overall system also needs to be modelled. These delays originate from TVC actuators, sensors and digital processing from on-board computers in general. In [19], each of these subsystems have a delay on 15 ms, 12 ms and 12 ms, respectively. This makes the total delay in the system 39 ms with ± 10 ms uncertainty [19]. This is represented by $\tau = \tau^0 + \sigma_\tau \delta_\tau$, where $\tau^0 = 39$ ms and $\sigma_\tau = 10$ ms. Figure 2.17A on the next page shows the upper LFT representation of the delay model, $G_\tau(s)$, where:

$$\Delta_\tau = I_4 \delta_\tau \quad (2.52)$$

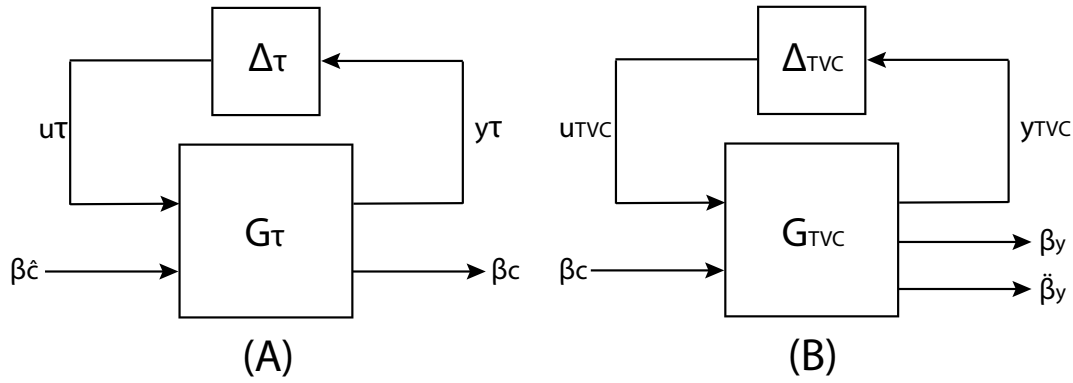


Figure 2.17: (A) showing the upper LFT representation of $G_\tau(s)$ and (B) showing the upper LFT representation of $G_{TV_C}(s)$.

In Figure 2.18, a 2nd order Padé approximation is designed to simulate the delays in the system, where the red line is representing the nominal delay in the system, and the gray lines are representing dispersed responses. Here it can be seen the gains are approximately 0 dB and provides overall good convergence with respect to pure time delay within the frequency range of interest for analysis and design.

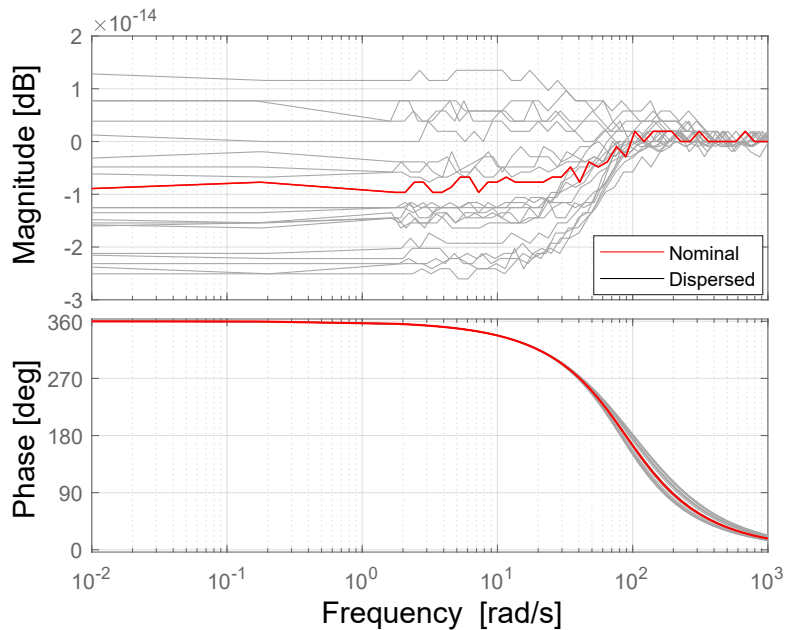


Figure 2.18: Nominal and dispersed frequency response of the delay model

2.12.5 Dryden Filter

The Dryden filter [28] is a mathematical model that is used to represent atmospheric turbulence. It colours white noise by transforming it into wind gusts where it treats it as spatially varying stochastic processes [29]. In Equation 2.53 the transfer function of the Dryden filter is shown [1] [8].

$$G_{\text{wind}}(s) = \frac{v_w(s)}{n_w(s)} = \frac{\sqrt{\frac{2}{\pi} \frac{V_w(h)}{L_w(h)} \sigma_w^2(h)}}{s + \frac{V_w(h)}{L_w(h)}} \quad (2.53)$$

where $L_w(h)$ is the turbulence scale and $\sigma_w(h)$ is the standard deviation of the wind turbulence. In [19] and [30], $L_w(h)$ and $\sigma_w(h)$ can be found in tabular form and can also be seen in Table 2.4. Here the standard deviation of the wind turbulence is defined for three wind conditions: Light, moderate, and severe. In this thesis, the standard deviation is set for light weather conditions, but will be scalable later in Section 4.4 when assigning weights to the LV models.

Altitude h [km]	Turbulence length scale L_w [m]	Wind standard deviation σ_w [m/s]		
		Light	Moderate	Severe
1	832	0.17	1.65	5.70
2	902	0.17	1.65	5.80
4	1040	0.20	2.04	6.24
6	1040	0.21	2.13	7.16
8	1040	0.22	2.15	7.59
10	1230	0.22	2.23	7.72
12	1800	0.25	2.47	7.89
14	2820	0.26	2.62	6.93
16	3400	0.24	2.44	5.00
18	5000	0.22	2.21	4.07
20	8640	0.23	2.26	3.85

Table 2.4: Turbulence length scale and wind standard deviation at different altitudes [19]

$V_w(h)$ is defined by a vertical profile of wind velocity. In this project, this wind profile has been inspired by [19] and can be seen in Equation 2.54. Beyond twenty kilometers the wind disturbance is not considered to have a significant impact on the LV anymore and the wind is therefore set to zero. For low altitudes the wind amplitude is not considered to be of any significance but gradually builds up with an exponential leading edge until $h = 2000$ m altitude. During intermediate altitudes between $2000 \text{ m} \leq h \leq 17500 \text{ m}$, the gust amplitude has been set to a constant of 14 m/s as this is also used in [19]. For the trailing edge, $V_w(h)$ decreases with a "1-cosine" function until the $V_w(h)$ reaches zero at $h = 20000$ m.

$$V_w(h) = \begin{cases} 10A \left[\left(\frac{h}{H_l} \right)^{0.9} - 0.9 \frac{h}{H_l} \right] & \text{for } 0 \leq h < H_l \\ A & \text{for } H_l \leq h \leq H_f - H_u \\ \frac{A}{2} \left[1 - \cos \left(\frac{\pi}{H_u} (h - H_f) \right) \right] & \text{for } H_f - H_u < h \leq H_f \\ 0 & \text{for } h > H_f \end{cases} \quad (2.54)$$

where $H_l = 2000$ m, $H_u = 2500$ m, $H_f = 20000$ m and $A = 14$ m/s.

Figure 2.19A shows how the $V_w(h)$ -coefficient changes over relevant altitudes. According to the simulation explained in subsection 1.3.1, the LV reaches twenty kilometers altitude at sixty seconds. Therefore Figure 2.19B shows the resulting Dryden filters from a time range between five to sixty-five seconds, as the Dryden filters above sixty seconds will just be zero.

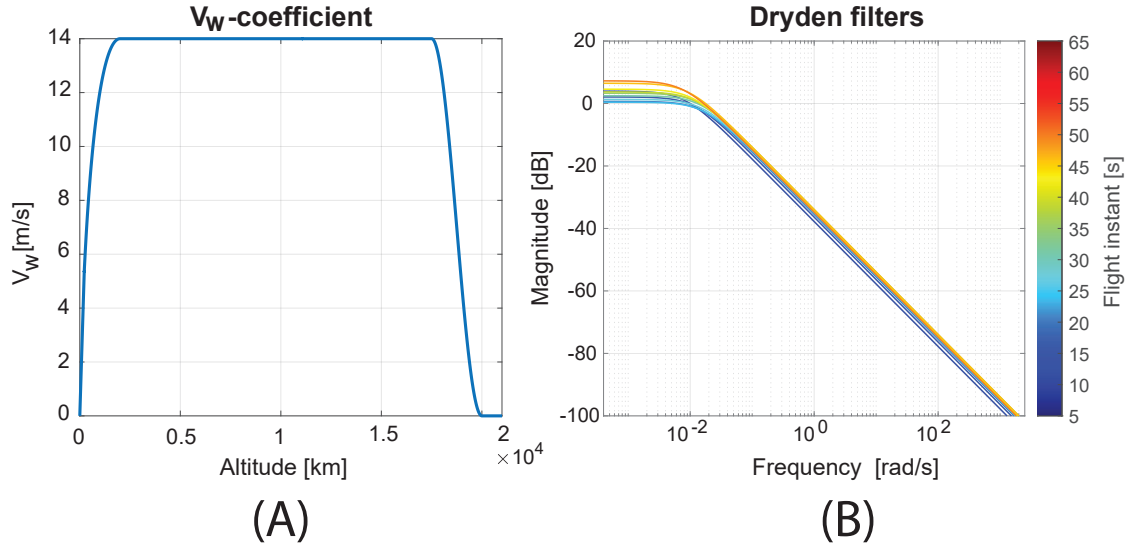


Figure 2.19: (A) shows the development of $V_w(h)$ from zero to twenty kilometers. (B) shows the resulting Dryden filters from different time instants of the LV flight.

2.13 Summary

Throughout Chapter 2 a model of an LV has been deduced with the VEGA launcher as a benchmark. In the beginning of this chapter, an overview of the VEGA LV model was introduced, and a trajectory profile provided by ESA was presented for the LV to follow. The necessary reference frames were described to later deduce the translational and rotational dynamic equations for an LV model in 3D. All the dynamical equations were evaluated by data representing the VEGA LV and was provided by ESA.

For simplicity, the 3D LV model was converted to a 2D model and Jacob linearizations were conducted in a systematically manner on the dynamic equations. The earlier introduced trajectory profile was then used for determining operating points so the linearization could be gridded along the trajectory profile. A state space system was established and frequency responses of LTI systems at different time instants concluded that the dynamics of the LV changes throughout the flight. The chapter ended with introducing uncertainties to the LV model, a TVC actuation model and a delay model with an upper LFT configuration. A wind disturbance model was also modelled in the end.

The next chapter will present technical requirements along with establishing performance requirements for the total LV system.

Requirement Specification 3

In the previous chapter the model of the LV was derived as well as the TVC model and the delay model. In this chapter the stability requirements and the performance requirements will be analyzed and evaluated upon.

3.1 Technical Requirements

In [1] [8] [19] and [27] there are descriptions of typical technical requirements for what a control system should achieve for an LV system. A summary of these requirements have been listed below and will be evaluated in the next section:

- *Stability:*
First and foremost the control system should be stabilized when accounting for disturbances.
- *Attitude Tracking:*
The control system should track attitude commands such that the error converges to zero.
- *Load and Drift Management:*
The control system should reduce the dynamic pressure and drift from the preprogrammed trajectory.
- *Actuation Minimization:*
TVC actuation during the flight should not reach its deflection and bandwidth limits.
- *Disturbance Rejection:*
Rejecting disturbances such as wind gusts, noise on sensors and internal dynamics such as bending modes.

Some of the requirements mentioned above are contradicting each other. For example, in order to minimize the aerodynamic load on the vehicle, the control system must pitch in the direction of the wind field, but in doing so makes the LV drift away from its preprogrammed trajectory. Therefore, a trade-off balance between load and drift is required [1].

3.2 Performance Requirements

As previously mentioned, the structural load is crucial for the LV to keep low. Recall Equation 2.18 on page 15 where the performance indicator Q_α was introduced: $Q_\alpha(t) = Q(t) \cdot \alpha(t)$. A performance requirement is made to keep its value below a certain envelope during the atmospheric flight. In Figure 3.1 this envelope can be seen, where Q_α is plotted as a function of the Mach number. The graph is an approximation from [19] and is assumed

to be sufficient to function as an upper bound of dynamic pressure and AoA for this thesis. In Figure 3.1, the bound on Q_α rises at around one and two Mach, which corresponds with where the dynamic pressure is at its highest during the flight.

Note that Q_α is sensitive to wind disturbances due to its dependency on the AoA. Therefore, the control system must be robust against wind gusts to keep the structural load below the certain threshold. Thereby, the load requirement also sets an indirect natural maximum limit on the AoA at different Mach numbers throughout the atmospheric flight. Therefore, there will be no requirement on a specific degree of maximum AoA.

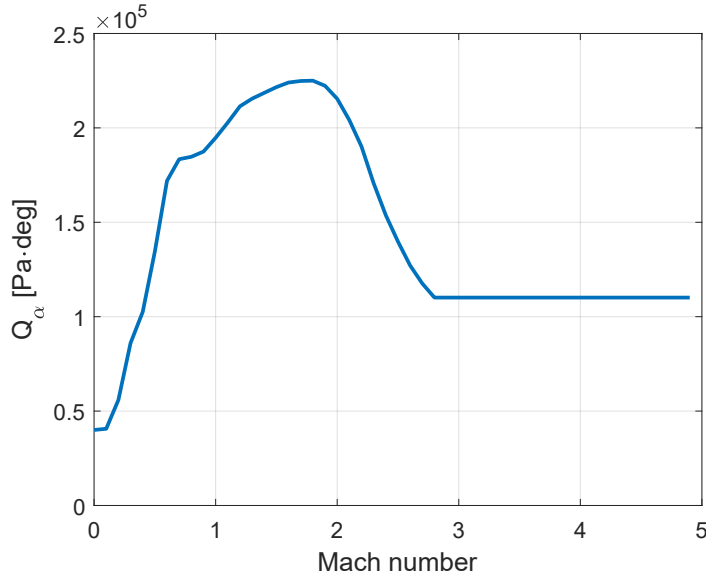


Figure 3.1: Q_α envelope [19]

To keep the structural load low, the LV will be allowed to drift from its predetermined trajectory. Requirements for the lateral drift and drift rate (z, \dot{z}) have been made to ensure that even if the LV drifts from its predefined trajectory, it will only do so within a certain range.

Lastly, a performance requirement is made to limit the actuation effort of the TVC actuators. This performance requirement ensures efficiency of fuel consumption by converting it into longitudinal velocity along the reference trajectory instead of gimballing the LV.

The performance requirements are summarized in Table 3.1.

Requirements	Metrics	Bounds
Load performance	Q_α	$< Q_\alpha$ envelope
Lateral control performance	Position (z)	< 500 m
	Velocity (\dot{z})	< 15 m/s
Actuation performance	β	$< 6.5^\circ$
	Integrated β	$< 250^\circ\text{s}$

Table 3.1: Performance requirements for the control system [1] [19] [31]

The technical requirements for a typical LV system have now been explained and the performance requirements have been described and evaluated. The next chapter will be about establishing a framework LV system and design a controller with the requirements from this chapter in mind.

Linear Parameter-Varying Control Design 4

This chapter will present the control system theory and design for the LV model derived back in Section 2.11 using the Linear Varying-Parameter synthesis. First, an introduction on why gridded LPV control is preferred over \mathcal{H}_∞ and other gain scheduling methods. Next, the modelling of the LPV in the LFT framework is introduced, then a brief overview of quadratic and robust stability is explained. Then the controller synthesis is described with a theorem, followed by assigning the time-varying parameter. An affine interpolation approach is presented before a weighted LFT-framework is designed for the LV system.

4.1 Introduction to LPV Theory

There exist different methods of designing an LPV controller. These include a grid-based LPV model and LFT-based modelling method that captures the behaviour of the time-varying parameters. Another approach is to have the system on polytopic form. This includes having the state space matrices that are depended on the time-varying parameter on affine form [32]. In this thesis the grid-based approach will be used.

As mentioned back in Section 2.10, the gain scheduling methodology is a standard practice to deal with systems with a wide dynamic variation and is also used in control of LVs [19]. The procedure is to have a number of linear designs at different operational points over the course of the atmospheric flight and design local linear controllers for each operational point. Then, a global controller will interpolate between the local controllers as the LVs dynamics change during the flight. The main drawback with gain scheduling, is that between the operational points there is no guarantee for stability. This is where linear parameter-varying control theory can be considered to extend the gain scheduling theory by guaranteeing stability. LPV control problems can be established by Linear Matrix Inequalities (LMIs) and Semidefinite Programming (SDP) is then used to solve the problems. By using LMIs the feasible solution to the control problem is also convex [33].

The LPV framework is in many ways, very similar to the standard \mathcal{H}_∞ framework. Firstly, they use the same LFT interconnection presented back in subsection 2.12.1. They both use control techniques that provide optimality and robustness. The LPV approach can be used for gain scheduling like the \mathcal{H}_∞ framework does. Since the LPV approach takes time-varying parameters in the system into account to establish the LMIs, it can be considered an augmentation of the \mathcal{H}_∞ approach.

4.2 LPV Modelling

A system with one or more varying parameters can be represented as a state space, but where the matrices are dependent on the varying parameters $\rho(t)$. In Equation 4.1 such a system can be seen.

$$\begin{bmatrix} \dot{x}(t) \\ y(t) \end{bmatrix} = \begin{bmatrix} A(\rho(t)) & B(\rho(t)) \\ C(\rho(t)) & D(\rho(t)) \end{bmatrix} \begin{bmatrix} x(t) \\ u(t) \end{bmatrix}, \quad \rho \in \mathcal{P} \quad \underline{\nu} \leq \dot{\rho} \leq \bar{\nu} \quad (4.1)$$

where $\mathcal{P} \subset \mathbb{R}^{n_\rho}$ is a known compact set which ρ belongs to. A , B , C and D are the continuous state-space matrices [1].

The varying parameter(s) are time-dependent. These parameters are defined as changing and initially unknown but causal, meaning they can be measured in real-time. Depending on the stability, the varying parameters $\rho(t)$ can also have defined bounds on their rate they are changing with: A minimum rate $\underline{\nu}$ and a maximum rate $\bar{\nu}$ [32].

When designing a controller with LPV synthesis, the objective is to find a linear controller $K(\rho)$, such that the Multiple-Input and Multiple-Output (MIMO) plant $P(\rho)$ meets the requirements specified back in Chapter 3. When designing the controller, the interconnection is the same as a lower LFT configuration, which also was introduced back in Figure 2.12 on page 29.

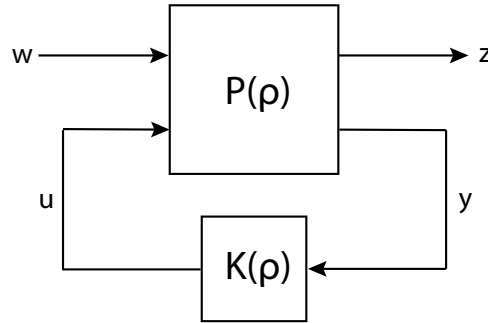


Figure 4.1: LPV control problem formulation [1]

The plant $P(\rho)$ is partitioned as shown below:

$$\begin{bmatrix} \dot{x} \\ z \\ y \end{bmatrix} = \underbrace{\begin{bmatrix} A(\rho) & B_1(\rho) & B_2(\rho) \\ C_1(\rho) & D_{11}(\rho) & D_{12}(\rho) \\ C_2(\rho) & D_{21}(\rho) & D_{22}(\rho) \end{bmatrix}}_{P(\rho)} \begin{bmatrix} x \\ w \\ u \end{bmatrix} \quad (4.2)$$

where x is the state vector of P , $x \in \mathbb{R}^{n_x}$, $y \in \mathbb{R}^{n_y}$, $w \in \mathbb{R}^{n_w}$ and $z \in \mathbb{R}^{n_z}$.

The controller $K(\rho)$ with n_x states can be written as:

$$\begin{bmatrix} \dot{x}_c \\ u \end{bmatrix} = \underbrace{\begin{bmatrix} A_c(\rho) & B_c(\rho) \\ C_c(\rho) & D_c(\rho) \end{bmatrix}}_{K(\rho)} \begin{bmatrix} x_c \\ y \end{bmatrix} \quad (4.3)$$

The controller can, together with the LPV model in Equation 4.2, be represented as the closed-loop system in Equation 4.4 [19].

$$\begin{bmatrix} \dot{x}_{clp} \\ z \end{bmatrix} = \underbrace{\begin{bmatrix} A_{clp}(\rho) & B_{clp}(\rho) \\ C_{clp}(\rho) & D_{clp}(\rho) \end{bmatrix}}_{\mathcal{T}_{zw}(\rho)=\mathcal{F}_l(P(\rho),K(\rho))} \begin{bmatrix} x_{clp} \\ w \end{bmatrix} \quad (4.4)$$

The induced \mathcal{L}_2 norm can be used as a performance metric that describes the maximum amplification of energy from the exogenous input w to the exogenous output z within the admissible set of scheduling time-varying parameters [19] [32]. In Equation 4.5, the \mathcal{L}_2 norm is expressed in terms of an LPV system [32]:

$$\begin{aligned} \|\mathcal{T}_{zw}(\rho)\|_{\mathcal{L}_2 \rightarrow \mathcal{L}_2} = & \sup_{\substack{\rho \in \mathcal{P} \\ \underline{\nu} \leq \dot{\rho} \leq \bar{\nu}}} \sup_{\substack{w \in \mathcal{L}_2 \\ \|w\|_{\mathcal{L}_2} \neq 0}} \frac{\|z\|_{\mathcal{L}_2}}{\|w\|_{\mathcal{L}_2}} \end{aligned} \quad (4.5)$$

The LPV synthesis problem then becomes choosing a controller $K(\rho)$ that minimizes the induced \mathcal{L}_2 norm subject to the time-varying parameters and the rate of change of these time-varying parameters. This control problem can be seen in Equation 4.6.

$$\min_{K(\rho)} \left\| \mathcal{F}_l(P(\rho), K(\rho)) \right\|_{\mathcal{L}_2 \rightarrow \mathcal{L}_2}; \quad \text{subject to } \begin{array}{l} \rho \in \mathcal{P} \\ \underline{\nu} \leq \dot{\rho} \leq \bar{\nu} \end{array} \quad (4.6)$$

Notion of Stability

The system is said to be quadratically stable if the problem is solved without the rated bounds on the time-varying parameters, meaning that $-\infty \leq \dot{\rho} \leq \infty$. Then the synthesis is performed by finding a single Lyapunov function [32]. To find a system that is quadratically stable is one of the simplest ways for LPV-control synthesis. However, the solution to the control problem is rather conservative compared to the robust synthesis. This is because stronger conditions requires to be satisfied before quadratic stability is achieved compared to the robust stability [32].

If the control problem in Equation 4.6 is rate-bounded, then a robust synthesis is carried out. Here, parameter dependent Lyapunov functions are employed to find an equal amount of parameter dependent controllers. This approach reduces the conservatism of the solution but is also a more complex and computationally demanding optimization process [19].

In Figure 4.2 an overview of stability is presented. Both quadratic stability and robust stability implies exponential stability. The quadratic stability is a special case of robust stability, hence quadratic stability implies robust stability, but not the other way around.

There exists systems which are Hurwitz but are not quadratically stable. The reader is advised to consult [32] for more information about stability of LPV systems.

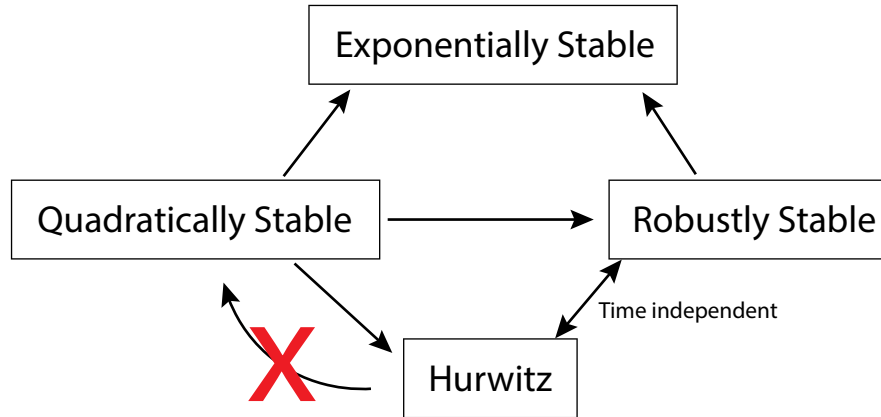


Figure 4.2: Overview of quadratic and robust stability

4.3 LPV Synthesis

In this section the controller synthesis is explained. The design strategy will be to design a robustly stable family of controllers with the gridding method for gain scheduling.

The LV system G_{LV} in Equation 2.44 on page 26 has a dynamic output, hence the according synthesis will be accounted for. As mentioned in Section 4.1, the control problem in Equation 4.6 can be described as an LMI problem. The optimization with robust stabilization by dynamic output feedback consists by employing parameter-dependent Lyapunov functions to find parameter-dependent controllers such that the theorem from [32] below is satisfied:

Theorem

Consider the LPV system together with the dynamic output feedback controller:

$$\begin{aligned} \dot{x}(t) &= A(\rho(t))x(t) + E(\rho(t))w(t) + B(\rho(t))u(t) \\ z(t) &= C(\rho(t))x(t) + F(\rho(t))w(t) + D(\rho(t))u(t) \\ y(t) &= C_y(\rho(t))x(t) + F_y(\rho(t))w(t) \end{aligned} \quad (4.7)$$

$$\begin{aligned} \dot{x}_c(t) &= A_c(\rho(t))x_c(t) + B_c(\rho(t))y(t) \\ u(t) &= C_c(\rho(t))x_c(t) + D_c(\rho(t))y(t) \end{aligned} \quad (4.8)$$

where $u \in \mathbb{R}^m$, $w \in \mathbb{R}^p$, $z \in \mathbb{R}^q$ and $y \in \mathbb{R}^r$.

Let M and the full-rank matrices $N_Y(\rho)$ and $N_X(\rho)$ be defined by:

$$\begin{aligned} [C_y(\rho) \quad F_y(\rho) \quad 0_{r \times q}] N_X(\rho) = 0, \quad N_Y(\rho)^T \begin{bmatrix} B(\rho) \\ D(\rho) \\ 0_{p \times m} \end{bmatrix} = 0, \quad (4.9) \\ M(\rho) = \begin{bmatrix} X_1(\rho) & I \\ \star & Y_1(\rho) \end{bmatrix} \end{aligned}$$

where \star means its transposed symmetric counterpart in the matrix and $N_X(\rho)$ and $N_Y(\rho)$ are chosen such that the span of vectors they are representing becomes the nullspace of the vectors in Equation 4.9.

The system in Equation 4.7 is robustly stabilizable by a dynamic output feedback controller on the form of Equation 4.8 if and only if there exists differentiable maps $X_1(\rho), Y_1(\rho) : \Delta_\rho \rightarrow S_{\rho_0}^n$ such that the LMIs:

$$N(\rho)_X^T \begin{bmatrix} He(X_1(\rho)A(\rho)) + \dot{X}_1(\rho) & X_1(\rho)E(\rho) & C(\rho)^T \\ \star & -\gamma I & F(\rho)^T \\ \star & \star & -\gamma I \end{bmatrix} N(\rho)_X \succ 0 \quad (4.10)$$

$$N(\rho)_Y^T \begin{bmatrix} He(A(\rho)Y_1(\rho)) - \dot{Y}_1(\rho) & Y_1(\rho)C(\rho)^T & E(\rho) \\ \star & -\gamma I & F(\rho) \\ \star & \star & -\gamma I \end{bmatrix} N(\rho)_Y \succ 0 \quad (4.11)$$

where:

$$\begin{aligned} He(\mathcal{H}) &= \mathcal{H} + \mathcal{H}^T, \\ \dot{Y}_1(\rho) &= \sum v_i \frac{\partial Y_1}{\partial \rho_i}(\rho), \\ \dot{X}_1(\rho) &= \sum v_i \frac{\partial X_1}{\partial \rho_i}(\rho), \\ M(\rho) &\succ 0 \end{aligned}$$

holds for all $(\rho, v) \in \Delta_\rho \times \text{vert}\{\Delta_\nu\}$

To ensure the system in Equation 4.7 is controllable and observable, the LMIs in Equation 4.10 and Equation 4.11 must hold, respectively.

The performance is given by:

$$\|\mathcal{T}_{zw}(\rho)\|_{\mathcal{L}_2 \rightarrow \mathcal{L}_2} \leq \gamma \quad \forall (w \in L_2, \rho \in \mathcal{P}^\nu), \mathcal{P}^\nu = \{\rho \in \mathcal{P} | \dot{\rho} \in \Delta_\nu\} \quad (4.12)$$

Once X_1 and Y_1 have been found from the LMIs, a procedure for computing the dynamic output feedback controller in Equation 4.8 can be found in [32] in proposition 3.3.8. This procedure must be done for each $\rho \in \Delta_\rho$, hence one needs to grid Δ_ρ in order for it to be implementable [34].

The robust synthesis is implemented in the MATLAB toolbox *LPVTools* [12] with the function *lpvsyn* with rate bounded conditions, which will be used in this project.

4.3.1 Choosing the Varying Parameter

In [1] an analysis was carried out to investigate which parameter of an LV has the biggest impact on the state space model. This was done to strategically assign parameters with most impact as the time-varying parameters. Since assigning all the changing variables as time-varying parameters will add a lot of complexity to the synthesis process and increase the computation time exponentially [32]. The way the analysis was carried out, was first to define the smallest and largest value of each parameter, and then changing a parameter's smallest value to its largest value for each parameter. The parameter with the largest relative change in singular value was found through all possible combinations. This analysis is assumed sufficient for the purpose of finding the parameters with most impact on the LV. Note that not all combinations of parameters of smallest and largest values are realistic for an ascent of an LV. For example, minimum air density and maximum mass is not a realistic scenario.

The parameter with the largest relative change in singular value was found to be the velocity. This is in line with back in subsection 2.12.2, where the velocity, v_x , was found to be the parameter that occurred most times in G_{LV} with a total of 24 times, where some of them were squared. For more information on the analysis, please consult to the reference.

A table with parameters that have the most relative effect on the singular value ranked from most to least can be seen in Table 4.1.

Parameter	Maximum Relative effect on σ (without single outlier)	Nr
Velocity	250e3	1
Inertia	10e3	2
Air density	2e3	3
Center of Gravity	19 (1.5)	4
Pitch	2.5 (1.3)	5
Mach number	1	6
Center of Pressure	0.35	7
Mass	0.2 (0.01)	8
Gravity	0.1 (0.02)	9

Table 4.1: Parameters which are affecting the LV system listed from most to least [1]

In this thesis, only the velocity, $v_x(t) = \rho(t)$, have been chosen as the time-varying parameter due to simplicity and because it has 25 times as large relative effect on the singular value compared to the second largest effect from the inertia. Choosing the velocity is in good accordance with the VEGA LV, which also has the velocity as the varying parameter [19].

4.3.2 Controller Synthesis

The velocity has been gridded nine times:

$\rho = [96, 229, 352, 468, 625, 835, 1103, 1425, 1771]$ m/s, which corresponds at the times $t = [10, 20, 30, 40, 50, 60, 70, 80, 90]$ s. This requires the LTI-models on the grid to have the same number of inputs and outputs [19].

From previous data of the partially non-linear simulation from [1], the velocity and the corresponding acceleration have been gathered. The data from this simulation is assumed to be representative for a typical VEGA LV model. The acceleration throughout the ascent from one second to a hundred seconds lies between $5.4 \text{ m/s}^2 < \dot{\rho} < 36.4 \text{ m/s}^2$.

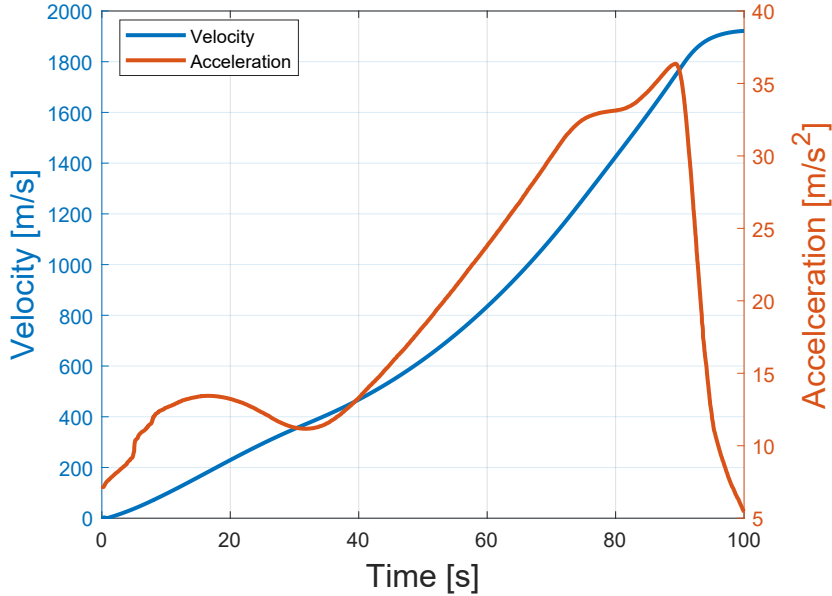


Figure 4.3: Velocity and acceleration from non-linear simulation

As mentioned earlier, the synthesis is carried out through the command *lpvsyn* with the MATLAB toolbox *LPVTools*. The rate variation of the velocity in the x-direction v_x , is included in the basis functions of X_ρ and Y_ρ . In this project, these basis functions are on quadratic form: $X_\rho = X_0 + X_1\rho + X_2\rho^2$ and $Y_\rho = Y_0 + Y_1\rho + Y_2\rho^2$. Through iterations of testing, quadratic basis functions have been found to yield good performance while keeping a relative low complexity for computational reasons. Furthermore, the critical dynamic pressure parameter, Q , depends on the square of the velocity.

Parametric Dependency on ρ

Traditionally, the other parameters in the state space matrix are independent of the velocity and therefore considered constant when gridding the state spaces. However, as mentioned back in Section 2.2 on page 7, the trajectory of the LV is predetermined in the atmospheric ascent phase. This makes the other parameters have a one-to-one relationship with the velocity and therefore possible to forecast what the other parameters are at any given velocity. This way, the other parameters can be considered functions of the velocity and the LPV model can account for the dynamics of all the parameters. This allows to grid the LTI-models presented back in Figure 2.11 on page 28 as they are with only one time-varying parameter.

Affine Interpolation

When the local controllers from the LTI models have been obtained, it has been chosen to make an affine interpolation between controllers between the given grid points. The affine

controllers are computed live as the LV ascents through the atmosphere. The resolution of affine controllers will be as high as the Nyquist frequency allows. The intention is to approximate a closer representation of controllers that would have been if a higher resolution than nine points were used. This is an attempt to get better performance while avoiding the disadvantages from more grid points, such as further conservatism and possible numerical problems from additional LMIs.

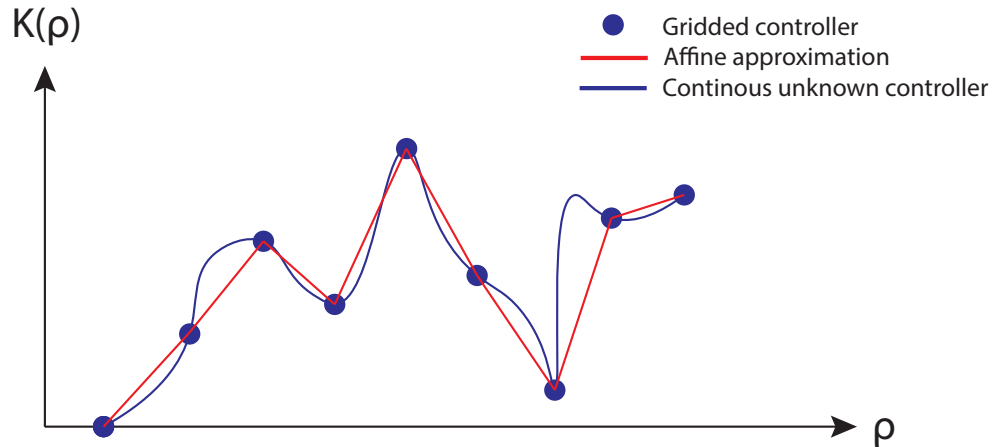


Figure 4.4: Illustration of affine interpolation between gridded controllers

The affine interpolation is made by obtaining data points from the longitudinal velocity v_x from the simulation mentioned back in subsection 1.3.1 to simulate measured data from a sensor. Then an affine regression is made between each of the nine gridded velocity points that are placed along the trajectory. The affine relationships between each gridded line are then used to interpolate between the controllers, resulting in the same number of controllers as there are data points between ten and ninety seconds of simulation.

4.4 Weighted Interconnection

In this section, the design of weights for the control system are explained with the intention of satisfying the established performance requirements from Chapter 3.

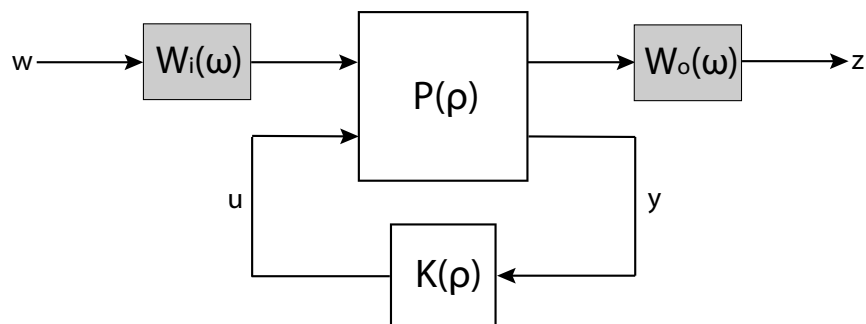


Figure 4.5: Weighted interconnection of the nominal LPV system

The lower LFT framework showed in Figure 4.1, can be augmented with input and output

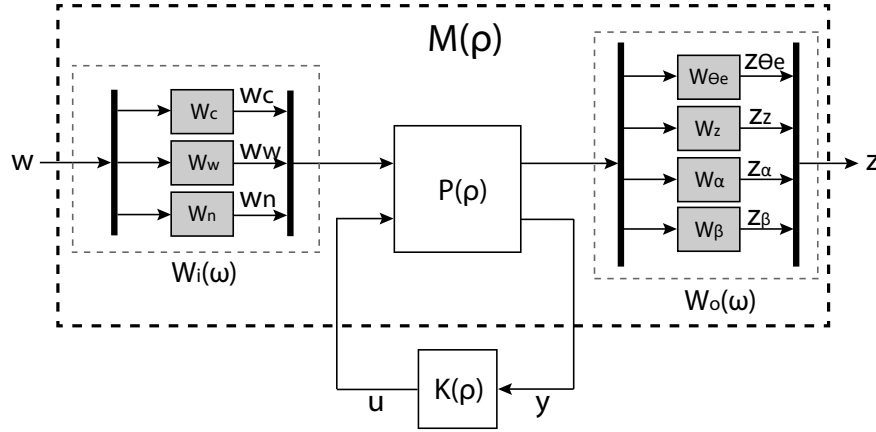


Figure 4.7: LFT closed-loop interconnection with weights

The input and output weight blocks have their weights partitioned as a diagonal in the LFT frame. This is shown in Equation 4.14 and Equation 4.15. The weights with four signals, i.e. W_c , W_n and W_z , have also their respective signals partitioned in a diagonal.

$$W_i = \begin{bmatrix} W_c & 0 & 0 \\ 0 & W_w & 0 \\ 0 & 0 & W_n \end{bmatrix} \quad (4.14)$$

$$W_o = \begin{bmatrix} W_{\theta_e} & 0 & 0 & 0 \\ 0 & W_z & 0 & 0 \\ 0 & 0 & W_\alpha & 0 \\ 0 & 0 & 0 & W_\beta \end{bmatrix} \quad (4.15)$$

Furthermore, this results in the closed-loop system of the lower LFT framework to be:

$$z = \mathcal{F}_l(M(\rho), K(\rho))w \quad (4.16)$$

4.5 Weighting Function Selection

Now that the interconnection of the weights has been accounted for, the selection of weights are evaluated. The weights will be chosen with the performance requirements in mind. Only the initial weights will be evaluated for, since the weighting function selection is typically an iterative process. The initial weights will be tuned until a desired response of the states have been met [19]. When choosing the weights, it is practical to use the same units for what comes into the weights and out of the weights. In this thesis, degrees and meters have been chosen for the angular and distance units for input and output signals respectively, since they are the same units given in the performance requirements. However, within the system radians will be used as angular units for designing the frequency dependent weights. Furthermore, since the LV in itself is already a complex system, the order of the weights have been kept low in order to reduce the complexity of the system $M(\rho)$ and ease the tuning in general. The theory of the weight selection have

been influenced from [1] and [19]. In the next two sections, the input weights and outputs weights are evaluated along with what the function of each weight is.

4.5.1 Input Weight Selection

Command Filters

The first weight to be considered is the command weight W_c , which have been placed on the input command w_c of the system. The command weights determine the maximum input a system can have. In this thesis the initial maximum commands for each signal has been set one:

$$W_c = \begin{bmatrix} W_{\theta_c} & 0 & 0 & 0 \\ 0 & W_{\dot{\theta}_c} & 0 & 0 \\ 0 & 0 & W_{z_c} & 0 \\ 0 & 0 & 0 & W_{\dot{z}_c} \end{bmatrix} = \begin{bmatrix} \frac{\pi}{180} & 0 & 0 & 0 \\ 0 & \frac{\pi}{180} & 0 & 0 \\ 0 & 0 & 1 & 0 \\ 0 & 0 & 0 & 1 \end{bmatrix} \quad (4.17)$$

Noise Filters

The noise on the sensors, W_n , have been provided by ESA and are set to 0.02° on the pitch, 0.01° per second on the pitch rate, drift noise is 0.01 m and for the drift rate the noise is 0.001 m/s [19].

$$W_n = \begin{bmatrix} \frac{\pi}{180}0.02 & 0 & 0 & 0 \\ 0 & \frac{\pi}{180}0.01 & 0 & 0 \\ 0 & 0 & 0.01 & 0 \\ 0 & 0 & 0 & 0.001 \end{bmatrix} \quad (4.18)$$

Wind Disturbance Filter

W_w is placed on the disturbance channel going into G_{wind} . The wind disturbance weight W_w scales the number of standard deviations of the velocity of the wind gusts produced by the Dryden filter [19] [36]. The number of standard deviations of wind gusts has been set to a constant of three across the whole trajectory, $W_w = 3$. Even though wind disturbances occur at relative low frequencies, it has been chosen to not implement a low-pass filter in W_w due to simplicity in the model

4.5.2 Output Weight Selection

For the output weight selection, the scaling introduced in Equation 4.13 is used. This means that the output weights will have the largest desired value of their respective parameters inverted in order to normalize the output to one: $z = \frac{\hat{z}}{\hat{z}_{\max}}$.

Sensitivity and Complementary Sensitivity filters

The first weights to be considered are W_{θ_e} and W_{θ_z} . These two weights are designed together and will be used to impose upper bounds on the sensitivity function $S_\theta(s)$ and the complementary sensitivity $T_\theta(s)$ function on the attitude channel, respectively. In this

design method, the so-called waterbed-effect will be utilized. This effect comes from the relationship: $S_\theta(s) + T_\theta(s) = 1$, which means that if the gain of $T_\theta(s)$ goes up, the gain of $S_\theta(s)$ is forced to go down in order to sum to one [35]. In this design, W_{θ_e} will be set to a constant and design a filter for $T_\theta(s)$ that vary over frequencies and having the gain of $S_\theta(s)$ vary in response of $T_\theta(s)$ [19]. By only having one transfer function with states reduces the complexity of the overall system.

W_{θ_e} penalizes the difference between the weighted commanded attitude input signal and the measured pitch signal $\theta_e = \theta_c - \theta_m$. W_{θ_e} will be designed to enforce stability on the attitude channel by setting a bound on the sensitivity function, $S_\theta(s)$, of that channel.

Lower values of $S_\theta(s)$ at low frequencies improves the reference tracking performance when disturbances are present. According to [37] and [19], sensitivity can be characterized by the nominal sensitivity peak: $\|S_\theta(s)\|_{\mathcal{L}_2}$.

As a consequence of penalizing the sensitivity function, W_{θ_e} is set to be:

$$W_{\theta_e} = \left(\frac{\pi}{180} \|S_\theta(s)\|_{\mathcal{L}_2} \right)^{-1} \quad (4.19)$$

Where the inverse of the sensitivity function comes from the normalization of output demonstrated in Equation 4.13. The inverse of W_{θ_e} ($W_{\theta_e}^{-1}$) will then impose an upper bound on $S_\theta(s)$. Normally when designing $S_\theta(s)$, $W_{\theta_e}^{-1}$ would have been chosen as a high-pass filter in order to keep the steady state tracking error low. Due to simplicity, W_{θ_e} is kept constant at 10 dB over all frequencies instead.

$$W_{\theta_e} = \left(\frac{\pi}{180} 3.16 \right)^{-1} \quad (4.20)$$

As for the inverse of the weight on the output on the attitude channel ($W_{\theta_z}^{-1}$), the weight impose an upper bound on the complementary sensitivity function, $T_\theta(s)$ on that channel. $W_{\theta_z}^{-1}$ is then shaped like a low-pass filter to limit the complementary sensitivity function at high frequencies.

$$W_{\theta_z}(s) = \left(\frac{\pi}{180} \frac{h_\theta s + \omega_\theta}{s + \frac{\omega_\theta}{l_\theta}} \right)^{-1} \quad (4.21)$$

To limit the tracking bandwidth, the crossover frequency is set to 10 rad/s: $\omega_\theta = 10$ rad/s. An attenuating high-frequency gain on -40 dB is implemented, in order to reduce the noise contribution from the sensors: $h_\theta = 0.01$. Lastly, the 10 dB gain of from the sensitivity function has been chosen on the low frequencies: $l_\theta = 3.16$.

The reason for using the gain of 10 dB at the low frequencies, is the relationship: $S_\theta(s) + T_\theta(s) = 1$. The sensitivity function $S_\theta(s)$ is forced to be under -10 dB at low frequencies because the $T_\theta(s)$ is 10 dB at low frequencies. This creates the desired trait of the sensitivity function of rejecting of disturbances [35].

LV State Filters

Regarding the weight on the attitude rate channel $W_{\dot{\theta}}$, there have been no requirements to this signal. As a consequence the weight on the channel has been set to zero: $W_{\dot{\theta}} = 0$.

The weights for the drift and drift rate are W_z and $W_{\dot{z}}$, respectively. Their inverse impose an upper bound for the maximum allowed value for drift and drift rate. Restricting the condition on these weights, will have the LV system lowering the total lateral drift, but will increase the structural load on the vehicle as a consequence. The initial values have been taken directly from the performance requirements in Section 3.2 since they are the largest allowed output [19]:

$$W_z = 500^{-1}, \quad W_{\dot{z}} = 15^{-1} \quad (4.22)$$

All the weights on the output have been covered and are partitioned in W_z like shown in Equation 4.23

$$W_z = \begin{bmatrix} W_{\theta_z} & 0 & 0 & 0 \\ 0 & W_{\dot{\theta}_z} & 0 & 0 \\ 0 & 0 & W_{z_z} & 0 \\ 0 & 0 & 0 & W_{\dot{z}_z} \end{bmatrix} \quad (4.23)$$

Q_α Performance Filter

$W_{Q_\alpha}(\rho)$ is the weighting function on the load requirement and is placed on the Q_α output channel from G_{LV} . For this weight, the dynamic pressure is updated for each gridded state space model, meaning it will be dependent on ρ . The purpose of this weight will restrict the maximum allowance on the AoA, which will be set to three degrees:

$$W_{Q_\alpha}(\rho) = \left(\frac{\pi}{180} Q(\rho) \alpha_{max} \right)^{-1} = \left(\frac{\pi}{180} 3Q(\rho) \right)^{-1} \quad (4.24)$$

Actuation Filter

Finally, the weight W_β is placed on the actuation channel. This weight will be designed to penalize the actuator saturation and thereby increasing fuel consumption efficiency. Moreover, by designing it like a low-pass filter, high frequency actuation is reduced.

$$LP_\beta(s) = \frac{h_u s + \omega_u}{s + \frac{\omega_u}{l_u}} \quad (4.25)$$

where h_u and l_u are high and low frequency asymptotes and ω_u is the actuation bandwidth. The low frequency asymptote, l_u is set to the maximum allowed actuator deflection: $l_u = \beta_{max} = 6.5^\circ$. β_{max} was stated in the performance requirements in Section 3.2 [19].

Additionally, to reduce the coupling between the actuator and the two bending modes, two notch filters have been designed to cancel out the bending modes. These notch filters

have been set in series with the low-pass filter. Since the frequency of the bending modes change for every flight instant, the notch filters have been designed to change along with the bending modes. The bandwidth of the two notch filters corresponds with the bandwidth of the first ($\omega_{q1}(\rho)$) and second bending mode ($\omega_{q2}(\rho)$), respectively.

The resulting actuation weight can be seen in Equation 4.26.

$$W_{\beta}(\rho) = \left(\frac{\pi}{180} \frac{s^2 + 0.5s + \omega_{q1}(\rho)^2}{s^2 + 70s + \omega_{q1}(\rho)^2} \cdot \frac{s^2 + 0.5s + \omega_{q2}(\rho)^2}{s^2 + 70s + \omega_{q2}(\rho)^2} \cdot \frac{0.01s + \omega_{q1}(\rho)}{s + \frac{\omega_{q1}(\rho)}{6.5}} \right)^{-1} \quad (4.26)$$

where the actuation bandwidth has been set equal to the bandwidth of the first bending mode: $\omega_u = \omega_{q1}(\rho)$. The frequency response of $W_{\beta}(\rho)^{-1}$ can be seen in Figure 4.8.

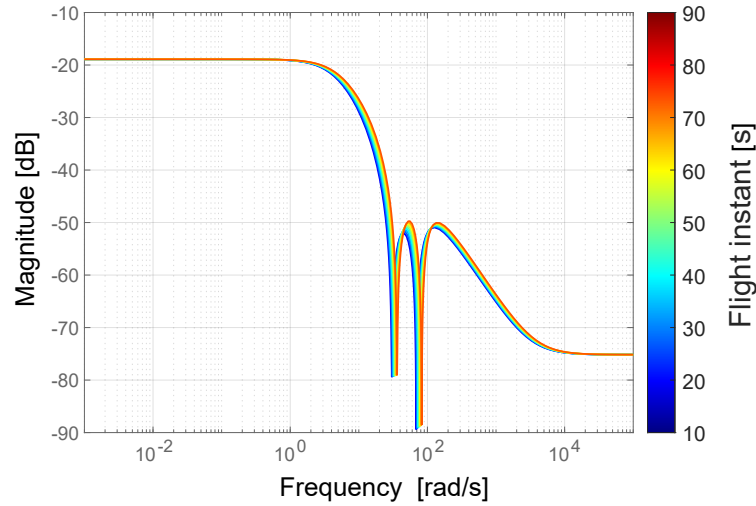


Figure 4.8: Frequency response of $W_{\beta}(\rho)^{-1}$. The low-pass filter and notch filters vary as the bending mode frequencies change over time.

To verify that $W_{\beta}(\rho)^{-1}$ does indeed cancel out the bending modes, a comparison has been plotted in Figure 4.9 on the next page. Figure 4.9A shows the open-loop frequency response of $\theta_z(\omega)/z_{\beta}(\omega)$ without $W_{\beta}(\rho)^{-1}$ and Figure 4.9B shows $\theta_z(\omega)/z_{\beta}(\omega)$ with $W_{\beta}(\rho)^{-1}$.

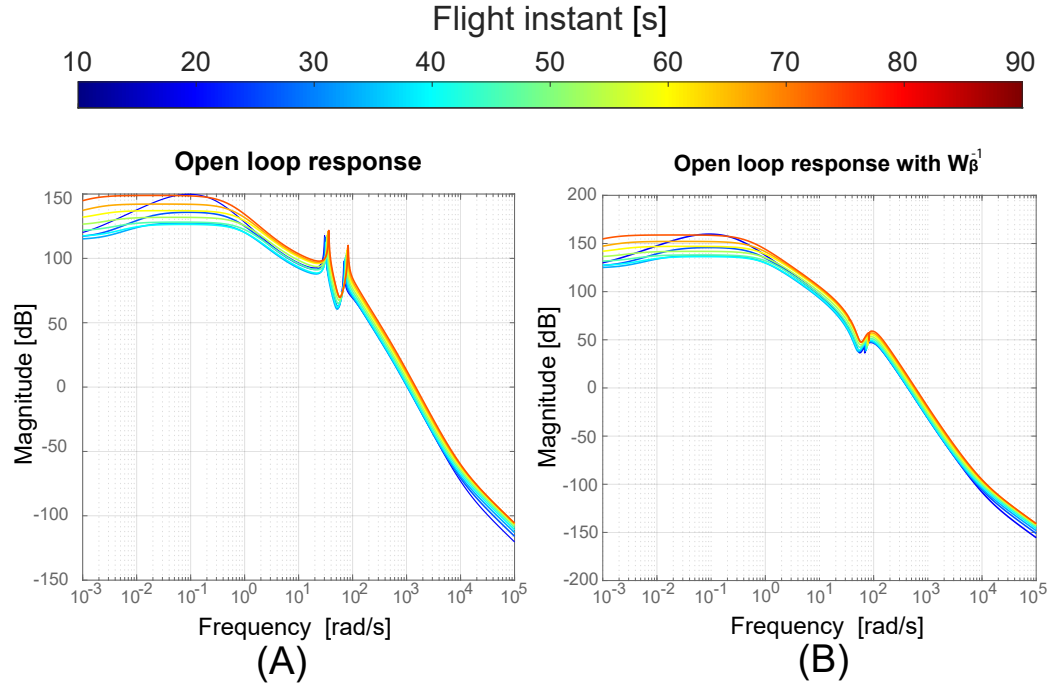


Figure 4.9: (A) shows the open-loop frequency response of $\theta_z(\omega)/z_\beta(\omega)$ of $M(\rho)$. (B) shows the open-loop frequency response of $\theta_z(\omega)/z_\beta(\omega)$ of $M(\rho)$ with $W_\beta(\rho)^{-1}$.

4.6 Summary

This chapter presented an overview of why gridded LPV control is a more sophisticated controller over other standard gain scheduling methods. Then the LPV modelling was described for a lower LFT configuration, together with an explanation that robust stabilization is preferred over quadratic stabilization for finding feasible solutions to the LPV control problem. Next, the theorem for output dynamic feedback for robust stabilization was accounted for. The longitudinal velocity v_x was chosen as the time-varying parameter of the system followed by an argument that the rest of the varying parameters in G_{LV} were dependent on the velocity with a one-to-one relationship. The idea of the affine interpolation between the gridded controllers has been presented and, lastly, the weighted interconnection compared to the requirements for the control system has been designed and evaluated.

The next chapter will present the results from the LPV synthesis conducted on $M(\rho)$ which was modelled in this chapter.

Results and Analysis 5

This chapter will present an analysis on the results from the robust LPV synthesis with dynamic output feedback that was conducted on the model designed in the previous chapter.

5.1 Results

The synthesis, carried out with *LPVTools*, does not allow to customize the structure of the resulting controllers. The resulting family of controllers have the structure as in Equation 4.3 and have 15 states, which is also the same number of states in the weighted interconnection $M(\rho)$ showed in Figure 4.7. The closed-loop system has 28 states. Note that the weights are only embedded in the controller and not in the plant used for the closed-loop system: $z = \mathcal{F}_l(P(\rho), K(\rho))w$.

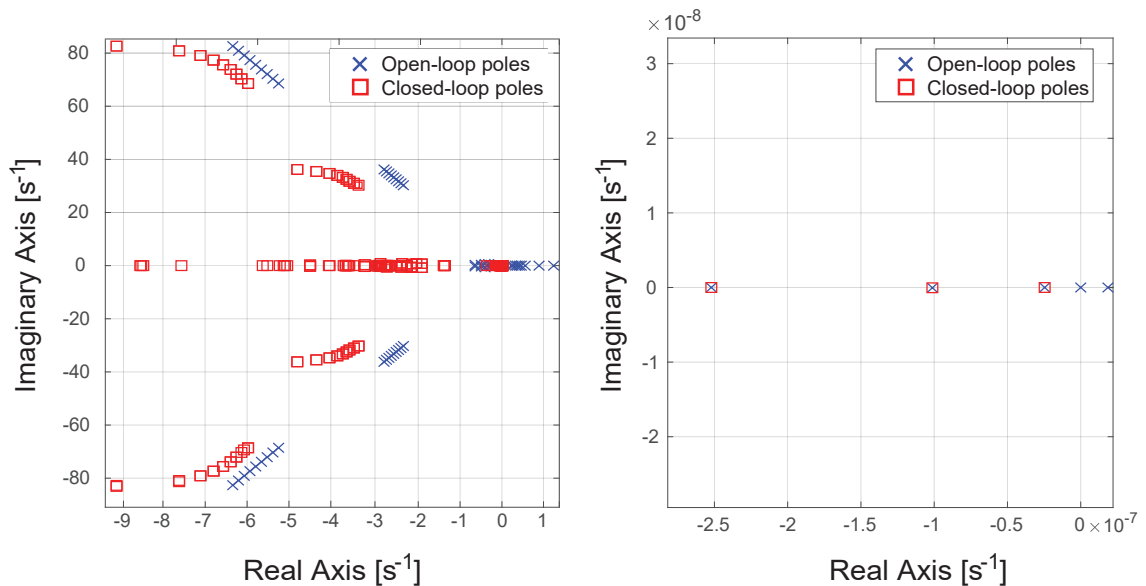


Figure 5.1: Poles of the LTI open-loop system and closed-loop system of the rigid and flexible states of the LV model

Above is a plot of the poles from the nine open-loop LTI systems and the nine closed-loop systems. The right plot is zoomed in around zero, to show that all the unstable poles have become stable. The internal poles and poles from the weights are not shown but are also stable. Note that because they are LTI systems, the closed-loop system is not guaranteed to be stable in between the gridded systems and therefore the LPV system is not guaranteed

to be stable either. Nonetheless, the stable LTI systems are a good indication for a stable LPV system, since they show stability with decent intervals throughout the flight time range.

Besides the controller, *lpvsyn* also computes the performance norm which highest possible value has been computed to be: $\gamma = 0.9807$. The performance norm is normalized because the output weights were normalized. Because the performance norm has been scaled, it informs if the requirements, represented by the weights, have been complied with. This is because γ is a supremum, meaning it represents the highest possible gain in the output channels. Recall back to the definition of the performance norm in Equation 4.12, where the norm can be lower or equal to γ . If $\gamma \leq 1$ then the requirements have been satisfied. However, if $\gamma > 1$ then it is possible that one or more output channels have been greater than the highest allowed value.

5.2 Simulation

The closed-loop LPV system $\mathcal{F}_l(P(\rho), K(\rho))$ is time-varying, so LTI analyses does not capture the time-varying nature of the model. Optimally, the control system would have been verified through a non-linear simulation, but as mentioned in Section 1.3, making such a simulation was not in the scope of this thesis. However, the function *lpvsim* provided by *LPVTools* [13], makes a linear time-domain simulation for a particular parameter trajectory, in this case the longitudinal velocity v_x . This simulation allows to evaluate the performance of an LFT controller $K(\rho)$, as the parameter varies with time. The simulation allows to set the states to initial values and capture the behavior of said state trajectories over a time period. Additionally, *lpvsim* also allows to insert user specified input to each input channel.

In Figure 5.2 on the next page, user specified inputs to each input channel are shown. The input on the command signals have been set to zero, meaning the controller will be feeded only with the output from the sensors. For the wind input, the signal has been set to a constant one. Lastly, the input signals on the noise have been chosen as Gaussian distributed signals scaled by their respective weights.

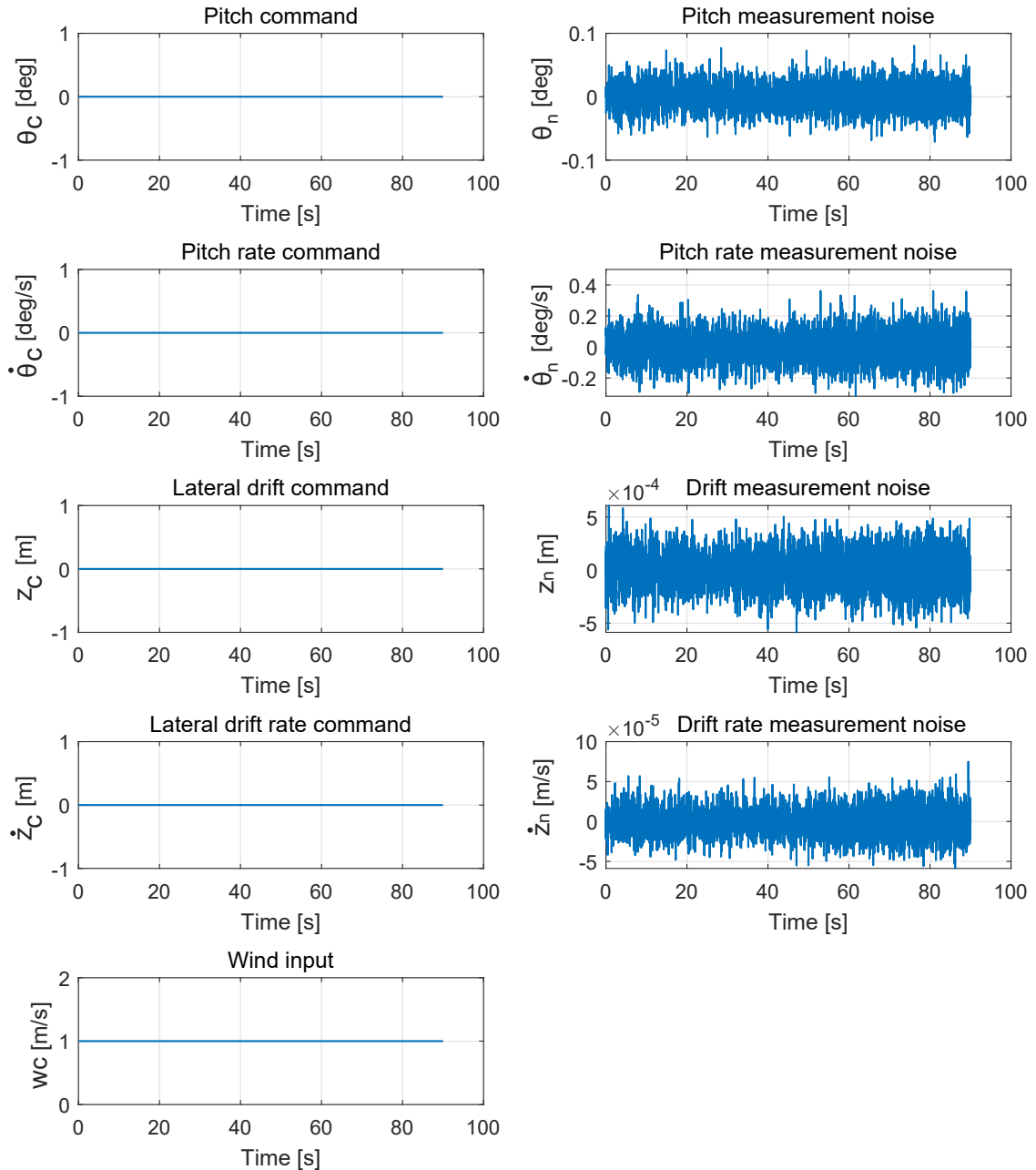


Figure 5.2: Input signals from the LPV simulation

The initial conditions on the 28 states have all been set to zero, except for the state representing the pitch angle, θ . This initial condition have been set to two degrees to simulate the control system align with the reference trajectory when a pitch angle different from zero is present. This is assumed to be a realistic value, since a separate controller could have been handled the pitch over manoeuvre and an error in the pitch is possible to occur when switching to the LPV controller.

The simulation output channels are shown in Figure 5.3. The first output shows the performance parameter Q_α . This parameter satisfies the requirement of not exceeding the upper bound showed back in Figure 3.1 on page 38. The next four outputs are the

rigid-body states, θ , $\dot{\theta}$, z and \dot{z} . As for their individual performance requirements, the pitch θ had an indirect requirement of not pitching in a way to make the AoA big enough to make Q_α exceed the maximum allowed value. There were no requirements specified for the pitch rate $\dot{\theta}$. Sanity checks on both the pitch and pitch rate indicates that they have values that represent a stable trajectory, since the highest pitch angle w.r.t. the trajectory is two degrees and highest pitch rate is two degrees per second. The lateral drift z must not exceed more than 500 m and the lateral drift rate \dot{z} must not exceed more than 15 m/s. Looking at the outputs for the drift and drift rates, these requirements have been satisfied as the maximum drift from the trajectory is 8 m and the maximum drift rate is 0.4 m/s.

The maximum signal for the actuation system has been measured to $z_\beta = 2.90^\circ$, and thereby does not exceed the maximum allowed actuation angle on 6.5° . Furthermore, the integration of the actuation signal has been measured to 0.4985°s and does not exceeded the requirement on 250°s .

Moreover, the pitch error output has been plotted and behaves as expected, i.e. it is the negative value of the pitch angle since the pitch command input is zero.

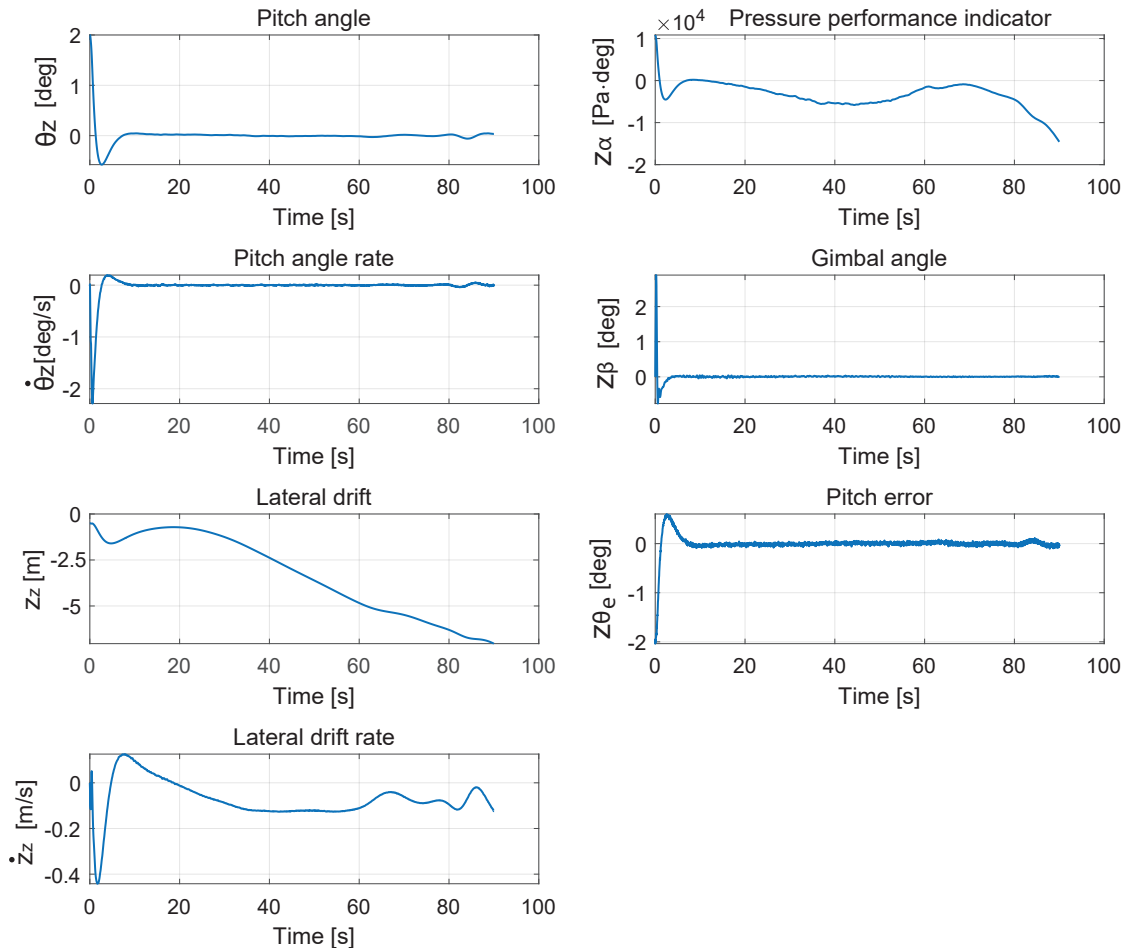


Figure 5.3: Output signals from the LPV simulation

The performance requirements from Section 3.2 have been summarized in Table 5.1, where

the measured values have been added and whether the respective requirements have been satisfied or not.

Requirements	Metrics	Bounds	Measured	✓/X
Load performance	Q_α	$< Q_\alpha$ envelope	$-14\,554.6^\circ\text{Pa}$	✓
Lateral control performance	Position (z)	< 500 m	-0.5002 m	✓
	Velocity (\dot{z})	< 15 m/s	0.1221 m/s	✓
Actuation performance	β	$< 6.5^\circ$	2.9281°	✓
	Integrated β	$< 250^\circ\text{s}$	0.4985°s	✓

Table 5.1: Performance requirements for the control system

5.2.1 Affine Interpolation

The affine interpolation, mentioned back in Section 4.3, has been carried out by first obtaining the 4037 data points of longitudinal velocity between ten and ninety seconds. Then an affine interpolation was carried out between each of the nine gridded velocity points that were placed along the trajectory.

Two comparisons between an LTI system and an affine approximated LPV system have been made to ensure the affine model captures the LV dynamics. The comparison can be seen in Figure 5.4. The comparisons are frequency responses captured at time instants different than the time instants used for the gridded LPV model. In the two comparisons, small differences can be seen between the LTI system and affine model at 35 seconds and 55 seconds but are considered negligible.

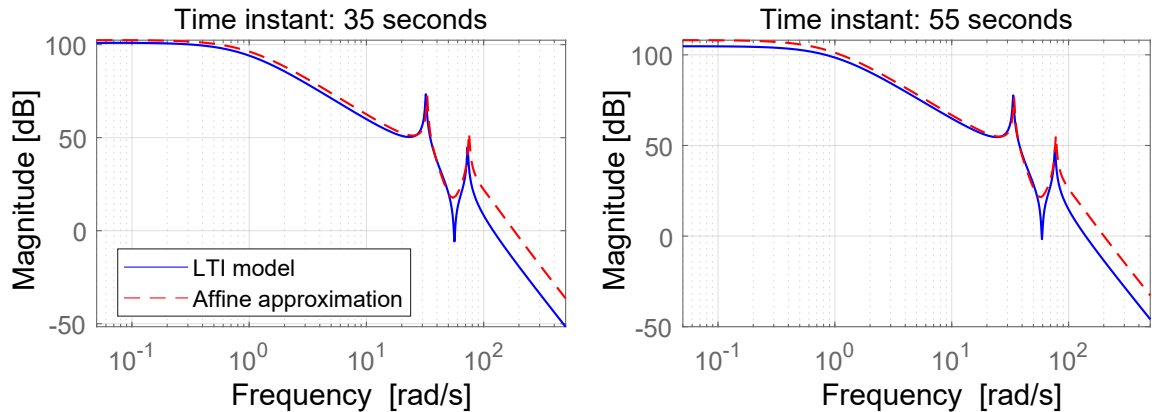


Figure 5.4: Affine model validation between LTI and affine models at time instants 35 seconds and 55 seconds, respectively

The results from the affine LPV model shows the same results as the gridded LPV model in the previous section. A further analysis of this phenomenon concluded that the function *lpvsim* does in fact also create an affine approximation of the gridded system in order to simulate the LPV model. Therefore, the exact same responses were given as the same method is used on the gridded LPV model.

5.3 Test Conclusion

This chapter presented all the closed-loop system poles for the LTI systems and showed they were stable. The normalized gain was computed to be less than one and thereby concluding that the output signals satisfies the requirements introduced in Chapter 3. An LPV simulation was conducted with specified inputs, where the requirements from Chapter 3 were verified to be satisfied by analyzing the output channels. Lastly, the affine LPV model was validated but showed the same results as the simulation with the gridded LPV model. The conclusion was that the simulation function *lpvsim* used the same affine approximation to run the LPV simulation.

This chapter concludes the results for the LPV control system for this thesis. The next chapter discusses the methods and choices made and the results in this report and ends with a conclusion of the overall thesis.

Conclusion 6

This chapter presents a discussion of the work done in the overall project and concludes the thesis in the end.

6.1 Discussion

6.1.1 LV Model

The LV model in this thesis was derived from an intuitive understanding of motions and rotations of the different dynamics affecting the LV instead of using an LV model from other scientific articles. Consequently, the LV model used in this project went through a lot of iterations, because it was forced to understand the individual parameters' influence on the overall complex model. This process was time consuming but gave a hands-on know-how understanding of LVs in general. Overall, the time on designing the model was well spent, even though more time on control theory might have resulted in a robust control system.

6.1.2 LPV Control

The LPV control system was synthesized with nine grid points from ten seconds to ninety seconds. This did not cover the whole flight period from zero to a hundred seconds, meaning there is no guarantee to have a stable LV outside the gridded time periods. While it is desirable to include the whole flight, doing so caused problems in finding feasible solutions to the control problem. The reason for this is expected to come from the radically change of dynamics at the start and the end of the flight. The thrust force differences between zero to ten seconds and ninety to a hundred seconds makes it troublesome to find a feasible solution to the control problem.

Additionally, since the gridding of velocity in this project corresponds with the velocity at every ten second time instant, the difference of velocity between each grid point increased due to an increasing acceleration. A more comprehensive way of gridding would have been to place grid points w.r.t. a certain constant change in velocity to average out the dynamical changes in the LV model. Unfortunately, it was proved difficult to find feasible solutions with this approach.

As for finding a feasible solution to the control problem, it was often a matter of tuning weights enough until a desired solution was achieved. Sometimes that meant a less conservative solution could be found but changing a decimal in just one of the weights resulted in an infeasible solution. The design method was to simplify the control problem

instead, by reducing the number of grid points and coverage of total flight period to allow a less conservative weight selection.

6.1.3 Extendable and Flexible Implementation of Code in MATLAB

A significant amount of time has been spent to make MATLAB code easier to extend in the future. Individual modules such as derivation of the LV model, acquiring LTI models and LPV synthesis can all work independently of each other. The simulation framework has also been designed to be extendable for future work. This is also the reason it was implemented with MATLAB, since ESA work with this programming language.

6.1.4 Future Work

This project can be considered as the first step towards making an LPV control system for an actual LV. However, there are still some important steps to make before implementing the control system into an actual LV system.

Firstly, Integral Quadratic Constraints (IQC) theory should be implemented in the LPV control system model to account for parameter uncertainties and other dispersions. Next, the control system should be tested in a full non-linear simulation to be certain if the control system can be implemented on a real LV. Before that is possible, the simulation would have to get verified. This can be done by testing individual dynamics, where an expected output is to be reached. A global controller for the gain scheduling will have to get implemented as well to interpolate between the gridded controllers. Lastly, the sophistication of the LPV controller can be extended to include the more varying parameters and include the full flight range from liftoff to MECO.

6.2 Conclusion

This master's thesis sought to develop an LPV controller, which guaranteed stability from liftoff to MECO of an LV's trajectory into orbit. The project was done in collaboration with ESA, who provided supervision and data from the VEGA LV. A 3D model of an LV was derived from relevant translation and rotational dynamic equations in the first half of Chapter 2. A 2D LV model was then linearized with Jacobian linearizations in a systematic manner. Together with the LV model, uncertain models of the TVC actuation system and delay model were introduced in an upper LFT configuration in the last part in Chapter 2. A family of controllers were designed with LPV synthesis in Chapter 4 w.r.t. established requirements of performance in Chapter 3. The closed-loop system was simulated in a linear simulation in Chapter 5 and showed results that satisfied the requirements. Thereby concluding the control system to be working as intended on an LV with the same parameters as the VEGA LV.

An affine LPV model was designed and simulated but showed no different results as with the gridded LPV model. The conclusion is that the LPV simulation used in this project uses the same affine approximation on the gridded LPV model when running the simulation.

The work done in this thesis can be considered as a springboard for new research in the future and overall is ESA very satisfied with the thesis.

Bibliography

- [1] Frederik Rasmussen, Jakob Stentoft Poulsen and Mikkel Damgård Hardysøe. \mathcal{H}_∞ - and lpv control for a modified vega launch vehicle in simulation, 2020.
- [2] Worldwide orbital launch summary by year. <http://www.spacelaunchreport.com/logyear.html>. Accessed: 2021-19-05.
- [3] Jonathan McDowell. Jonathan’s space report. <https://planet4589.org/space/log/launchlog.txt1>. Accessed: 2021-05-19.
- [4] Timeline of spaceflight. https://en.wikipedia.org/wiki/Timeline_of_spaceflight. Accessed: 2021-05-19.
- [5] Garrett Reisman. Statement of garrett reismandirector of crew operations space exploration technologies corp. (spacex). *Journal of spacecraft and rockets Vol. 33, No. 2*, 2015.
- [6] I-Shih Chang. Investigation of space launch vehicle catastrophic failures. *JOURNAL OF SPACECRAFT AND ROCKETS Vol. 33, No. 2*, 1996.
- [7] The tyranny of the rocket equation. https://www.nasa.gov/mission_pages/station/expeditions/expedition30/tryanny.html. Accessed: 2021-20-05.
- [8] P.V.M. Simplicio. *Guidance and Control Elements for Improved Access to Space: From Planetary Landers to Reusable Launchers*. University of Bristol, 2019.
- [9] Satellite communication - launching. https://www.tutorialspoint.com/satellite_communication/satellite_communication_launching.htm. Accessed: 2021-20-05.
- [10] Gary Balas, Richard Chiang, Andy Packard and Michael Safonov. *Robust Control Toolbox™ 3 - User’s Guide*. The MathWorks, 2009.
- [11] C Roux and I Cruciani. Scheduling schemes and control law robustness in atmospheric flight of vega launcher. In *Proceedings of the 7th ESA International Conference on Spacecraft Guidance, Navigation and Control Systems*, pages 1–5, 2008.
- [12] Arnar Hjartarson, Peter Seiler, and Andrew Packard. Lpvttools: A toolbox for modeling, analysis, and synthesis of parameter varying control systems. *IFAC-PapersOnLine*, 48(26):139–145, 2015. 1st IFAC Workshop on Linear Parameter Varying Systems LPVS 2015.
- [13] Gary J. Balas, Andrew Packard, Peter J. Seiler and Arnar Hjartarson. *LPVTools - A Toolbox for Modeling, Analysis, and Synthesis of Parameter Varying Control Systems*. MUSYN Inc., 2015.

-
- [14] A matlab project of a linear varying control (lpv) control system for a launch vehicle (lv). https://github.com/JakePoulsen/launch_vehicle_lpv. Accessed: 2021-27-05.
- [15] Vega launcher makes first flight. <https://www.bbc.com/news/science-environment-16956324>, note = Accessed: 2021-18-05.
- [16] Types of orbits. http://www.esa.int/Enabling_Support/Space_Transportation/Types_of_orbits#SS0, note = Accessed: 2021-18-05.
- [17] Communication Department ESA Media Relations Office. Press kit - vega qualification flight vv01. 2012.
- [18] Avio. Vega satellite launcher. https://web.archive.org/web/20141101022341/http://www.avio.com/files/catalog/pdf/avum_78.pdf. Accessed: 2021-05-16.
- [19] D. Navarro-Tapia. Robust and adaptive tvc control design approaches for the vega launcher. 2019.
- [20] ESA. The european small launcher. <https://www.esa.int/esapub/br/br257/br257.pdf>. Accessed: 2021-04-14.
- [21] How fast is the earth moving? <https://www.scientificamerican.com/article/how-fast-is-the-earth-mov/>, note = Accessed: 2021-15-02.
- [22] Wei Du. Dynamic modeling and ascent flight control of ares-i crew launch vehicle, 2010.
- [23] Arthur L Greensite. *Analysis and design of space vehicle flight control systems*, volume 15. Spartan books New York, 1970.
- [24] Rick Newlands, Martin Heywood and Andy Lee. Rocket vehicle loads and airframe design. Technical report, Aspirespace, 2016.
- [25] Jeb S. Orr, Matthew D. Johnson, Jonathan D Wetherbee and James H. McDuffie. State space implementation of linear perturbation dynamics equations for flexible launch vehicles. *AIAA Guidance, Navigation, and Control Conference*, 2009.
- [26] Sang-Il Leea, Jaemyung Ahn and Woong-Rae Roh. Integrated design optimization of structural bending filter and gain schedules for rocket attitude control system, 2018.
- [27] Pedro Simplicio, Samir Bennani, Xavier Lefort, Andres Marcos and Christophe Roux. Structured singular-value analysis of the vega launcher in atmospheric flight. *American Institute of Aeronautics and Astronautics Inc. (AIAA)*, 2016.
- [28] H. W. Liepmann. On the application of statistical concepts to the buffeting problem. 1952.
- [29] Dryden wind turbulence model. https://en.wikipedia.org/wiki/Dryden_Wind_Turbulence_Model, note = Accessed: 2021-23-05.
- [30] Dale L. Johnson and William W. Vaughan. Terrestrial environment (climatic) criteria handbook for use in aerospace vehicle development. 2004.

- [31] Structured h-infinity and linear parameter varying control design for the vega launch vehicle. September 2017. Eucass - 7th European Conference for Aeronautics and Space Sciences ; Conference date: 03-07-2017 Through 06-07-2017.
- [32] Corentin Briat. *Linear Parameter-Varying and Time-Delay Systems*. Springer, 2015.
- [33] Pablo Parrilo. Lyapunov equations and inequalities. duality in convex optimization and systems theory. linear matrix inequalities (lmi). s-procedure and applications (ellipsoid containment, etc.), May 2014.
- [34] John-Josef Leth. Stability and performance of lpv systems. 2020.
- [35] Sigurd Skogestad and Ian Postlethwaite. *Multivariable feedback control: analysis and design*, volume 2. Wiley New York, 2005.
- [36] Diego Navarro-Tapia, Andres Marcos, Samir Bennani, and Christophe Roux. Performance and robustness trade-off capabilities for the vega launcher tvc system. July 2019. European Conference for Aeronautics and Space Sciences, EUCASS 2019 ; Conference date: 01-07-2019 Through 04-07-2019.
- [37] K. Aström and T Hägglund. *PID Controllers: Theory, Design and Tuning*. Springer, 1995.

Parameters from Simulation

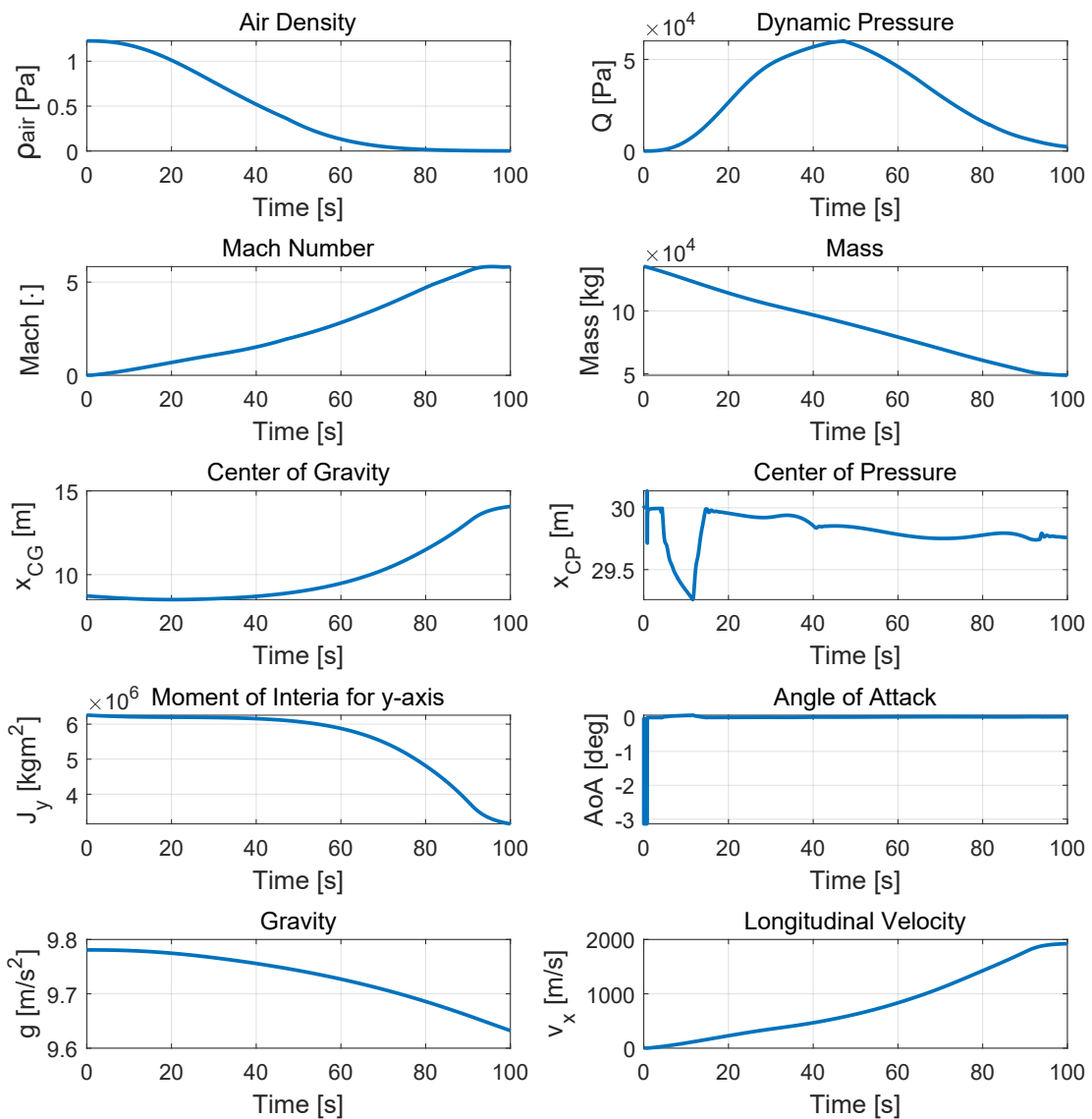


Figure A.1: Graphs of all used parameters from the partly non-linear simulation from [1]